AGU PUBLICATIONS

Geochemistry, Geophysics, Geosystems

RESEARCH ARTICLE
10.1002/2015GC006184

Thermo-kinematic evolution of the Annapurna-Dhaulagiri Himalaya, central Nepal: The Composite Orogenic System

A. J. Parsons[1], R. D. Law[2], G. E. Lloyd[1], R. J. Phillips[1], and M. P. Searle[3]

[1]School of Earth and Environment, University of Leeds, Leeds, UK, [2]Department of Geosciences, Virginia Tech, Blacksburg, Virginia, USA, [3]Depertment of Earth Sciences, University of Oxford, South Parks Road, Oxford, UK

Key Points:
- Three-stage evolution of GHS from midcrustal emplacement to upper crustal exhumation is revealed
- Channel flow, wedge extrusion, and duplexing all integral to development of Himalayan orogen
- Himalaya forms a Composite Orogenic System with spatially variable rheological boundary conditions

Supporting Information:
- Supporting Information S1
- Data Set S1
- Data Set S2
- Data Set S3
- Data Set S4

Correspondence to:
A. J. Parsons,
andrew.parsons@canada.ca

Citation:
Parsons, A. J., R. D. Law, G. E. Lloyd, R. J. Phillips, and M. P. Searle (2016), Thermo-kinematic evolution of the Annapurna-Dhaulagiri Himalaya, central Nepal: The Composite Orogenic System, *Geochem. Geophys. Geosyst.*, *17*, 1511–1539, doi:10.1002/2015GC006184.

Received 20 NOV 2015
Accepted 21 MAR 2016
Accepted article online 24 MAR 2016
Published online 30 APR 2016

Abstract The Himalayan orogen represents a "Composite Orogenic System" in which channel flow, wedge extrusion, and thrust stacking operate in separate "Orogenic Domains" with distinct rheologies and crustal positions. We analyze 104 samples from the metamorphic core (Greater Himalayan Sequence, GHS) and bounding units of the Annapurna-Dhaulagiri Himalaya, central Nepal. Optical microscopy and electron backscatter diffraction (EBSD) analyses provide a record of deformation microstructures and an indication of active crystal slip systems, strain geometries, and deformation temperatures. These data, combined with existing thermobarometry and geochronology data are used to construct detailed deformation temperature profiles for the GHS. The profiles define a three-stage thermokinematic evolution from midcrustal channel flow (Stage 1, >700°C to 550–650°C), to rigid wedge extrusion (Stage 2, 400–600°C) and duplexing (Stage 3, <280–400°C). These tectonic processes are not mutually exclusive, but are confined to separate rheologically distinct Orogenic Domains that form the modular components of a Composite Orogenic System. These Orogenic Domains may be active at the same time at different depths/positions within the orogen. The thermokinematic evolution of the Annapurna-Dhaulagiri Himalaya describes the migration of the GHS through these Orogenic Domains and reflects the spatial and temporal variability in rheological boundary conditions that govern orogenic systems.

1. Introduction

Identifying how the Himalayan metamorphic core deformed through dynamic PTt space is fundamental to understanding the orogen's kinematic evolution. In this study, we highlight the dominant role of rheology during the Himalayan orogeny and demonstrate that channel flow [e.g., *Beaumont et al*., 2001; *Godin et al*., 2006], wedge extrusion [e.g., *Burchfiel and Royden*, 1985], and duplexing/thrust stacking [e.g., *Robinson et al*., 2006; *Montomoli et al*., 2015], were *all* integral processes during structural development of the Himalaya.

Himalayan orogenesis is typically explained with one of three generalized end-member models: (1) channel flow [e.g., *Beaumont et al*., 2001; *Law et al*., 2004; *Searle et al*., 2003, 2006, 2010], (2) wedge extrusion [e.g., *Burchfiel and Royden*, 1985; *Burchfiel et al*. 1992], and (3) duplex/thrust stacking [e.g., *Robinson et al*., 2006; *Carosi et al*., 2010; *Montomoli et al*., 2013, 2015]. Channel flow models assume that the Himalayan metamorphic core (Greater Himalayan Sequence, GHS) formed as a partially molten, rheologically weak subhorizontal layer, which "flowed" southward relative to the upper and lower crust. Flow was driven by topographic overburden, underthrusting, and focused erosion. Wedge extrusion models consider the GHS to have formed as a wedge of midcrustal material, exhumed as a rigid block via top-SW thrusting on the underlying Main Central Thrust and gravitationally driven top-NE normal sense motion along the overlying South Tibetan Detachment; note that ductile wedge models of *Grujic et al*. [1996] and *Grasemann et al*. [1999] are early variants of the channel flow model. Duplex/thrust stacking models assume that the GHS represents a thrust stack within an orogen-scale duplex that was exhumed via thrust stacking of underlying crustal material.

All three end-member models have been proposed as possible explanations for the tectonic evolution of the Annapurna-Dhaulagiri Himalaya, central Nepal [*Hodges et al*., 1996; *Larson and Godin*, 2009; *Corrie and Kohn*, 2011] and distinction between them is difficult due to their a posteriori nature. An exception to this is the predicted deformation modes of each end-member model. During channel flow, deformation of the GHS is characterized by horizontal stretching and vertical shortening. Pervasive general shear (i.e., involving

components of both coaxial and noncoaxial flow) occurs throughout the GHS, aided by the rheological weakening effects of syntectonic partial melting [*Grujic*, 2006]. In contrast, rigid wedge and duplex/thrust stacking models are characterized by horizontal shortening and vertical thickening. In such models, the GHS is required to be rheologically strong in order to localize deformation on discrete bounding shear zones and promote duplex culmination [e.g., *Robinson et al*., 2006; *Carosi et al*. 2010; *Montomoli et al*., 2015]. From this perspective, rigid wedge models and duplexing/thrust stacking models are not so dissimilar, although the latter is explicit in the operation of thrust staking and duplex culmination as a means of exhumation for the GHS.

We present new microstructural data from the GHS and its bounding units in the Annapurna-Dhaulagiri Himalaya, central Nepal (Figure 1) to distinguish between these deformation modes and assess their validity. Optical microscopy was conducted on 104 samples from orogen-perpendicular transects situated along the Kali Gandaki and Modi Khola valleys. Microstructural observations are used to identify active crystal plastic deformation mechanisms in the context of local petrology and field observations. Specific temperature-dependent deformation mechanisms provide constraints on the temperature ranges at which deformation occurred [e.g., *Burkhard*, 1993; *Kruhl*, 1998; *Stipp et al*., 2002]. Scanning Electron Microscopy (SEM) Electron Backscatter Diffraction (EBSD) analysis was performed on 93 of these samples to determine Crystallographic Preferred Orientations (CPOs) of quartz, calcite, dolomite, plagioclase feldspar, and K-feldspar. These data are used to infer active crystal slip systems, deformation temperature ranges and strain kinematics and geometries [e.g., *Cole et al*., 2007; *Barth et al*., 2010; *Little et al*., 2013]. Photomicrographs of key microstructures used to support our findings and interpretations are presented as figures in this manuscript. Additional photomicrographs which support these figures are presented in the supporting information, cited with an '*S*' notation in front of the figure number (e.g., supporting information Figure S1). All CPO fabrics used to support our findings and interpretations are presented in supporting information cited as supporting information Data sets S2–S4. From these data sets, a selection of "type examples" of CPO fabrics are presented as figures in this manuscript.

Combining these results with previously published thermobarometric and chronometric constraints provides a detailed record of the thermokinematic evolution of the GHS in the Annapurna-Dhaulagiri Himalaya from midcrustal extrusion to late-stage exhumation. Our findings suggest that the Himalayan orogen is best described as a "Composite Orogenic System" in which channel flow, wedge extrusion, and duplexing/thrust stacking occur in distinct "Orogenic Domains" (perhaps contemporaneously) at different crustal positions with contrasting rheologies. These results support recently published composite models of Himalayan orogenesis that combine multiple orogenic processes into a single system [see *Cottle et al*., 2015; *Searle*, 2015 reviews].

1.1. Overview of the Annapurna-Dhaulagiri Himalaya

Crustal thickening within the Himalayan orogen began at ~50 Ma during final closure of Neotethys and has sustained a continuous state of convergence since that time [*Searle*, 1986; *Searle et al*., 2011]. In the Annapurna-Dhaulagiri Himalaya, central Nepal (Figure 1), the GHS is juxtaposed above the Lesser Himalayan Sequence (LHS) by the Main Central Thrust (MCT; top-SW) and below the Tethyan Himalayan Sequence (THS) by the South Tibetan Detachment (STD; top-down-NE) [*Le Fort*, 1975; *Colchen et al*., 1986; *Hodges et al*., 1996; *Searle and Godin*, 2003; *Searle*, 2010; *Parsons et al*., 2016a, 2016b]. *Parsons et al*. [2016b] and references therein provide detailed lithological and structural descriptions of the Annapurna-Dhaulagiri Himalaya, which we summarize below.

Following the regional geological map of *Parsons et al*. [2016a], the GHS is divided into the Lower GHS (LGHS), Upper GHS (UGHS), and South Tibetan Detachment System (STDS) (Figure 1). The LGHS and UGHS are separated by the Chomrong Thrust (CT; top-SW), while the UGHS and STDS are separated by the Annapurna Detachment (AD; top-down-E) and Deurali Detachment (DD; top-down-NE) in the Kali Gandaki and Modi Khola valleys, respectively (Figure 1). Additionally, the UGHS is cut by the out-of-sequence Kalopani and Modi Khola shear zones in the Kali Gandaki and Modi Khola valleys [*Hodges et al*., 1996; *Vannay and Hodges*, 1996; see also general reviews by *Montomoli et al*. [2015] and *Mukherjee* [2015] of structural discontinuities in the GHS of the central eastern Himalaya and their age relations]. A regional-scale tectonic foliation associated with extrusion of the GHS dips ~20–40°NE, parallel to the bounding shear zones (S3 of *Godin* [2003]; *Parsons et al*. [2016a]). Associated mineral stretching lineations (L3) plunge 20–40°N to NE in

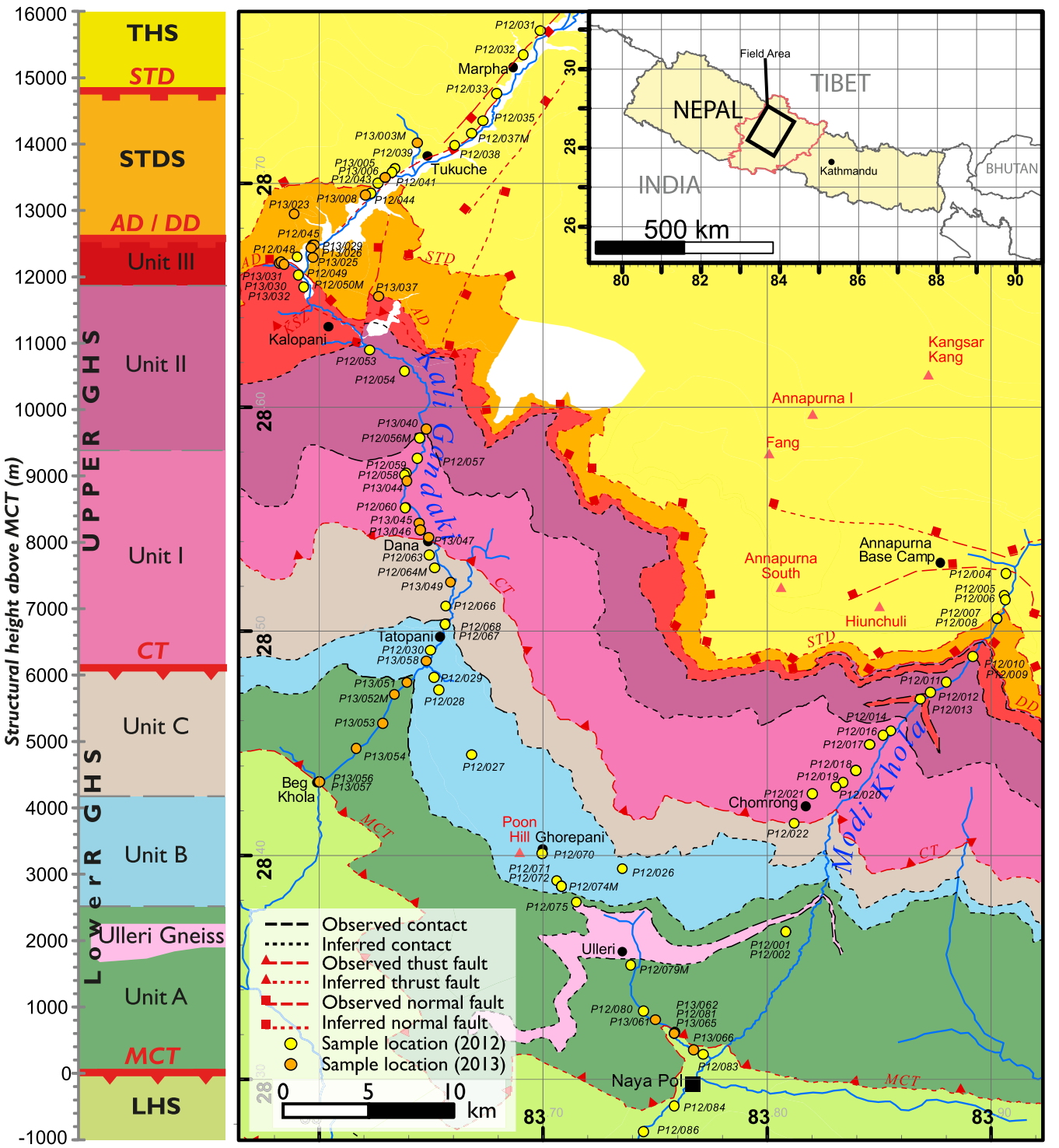

Figure 1. Geological map of the Annapurna-Dhaulagiri Himalaya. Tectonostratigraphic column for the Kali Gandaki transect presented to left of map.

the LGHS and lower UGHS and 20–30°NE to ESE in the upper UGHS and STDS [*Godin*, 2003; *Parsons et al.*, 2016a].

The LHS contains quartzites and metapelitic rocks that have been metamorphosed up to chlorite grade. The LGHS contains lower to upper greenschist facies metasedimentary rocks, divided into Units A, B, and C, listed from bottom to top (Figure 1). Unit A contains inter-bedded quartzites, pelites, semipelites, and the

laterally discontinuous Ulleri orthogneiss. Unit B contains quartzites and dolomitic marble (marble defined as >80% carbonate). Unit C consists of interbedded dolomitic metacarbonates (metacarbonate defined here as >50–80% carbonate) and calc-pelitic metasedimentary rocks. The UGHS contains amphibolite facies migmatites, schists, gneisses, and leucogranites and is divided into Units I, II, and III (Figure 1). Unit I comprises kyanite-bearing schists, paragneisses, and migmatites. Unit II contains clinopyroxene-bearing calc-silicate gneisses. Unit III contains kyanite-bearing migmatite and orthogneiss with subordinate sillimanite-bearing schists and calc-silicate layers. Leucosomes and leucogranite dykes and sills are observed across the UGHS and often contain kyanite, but not sillimanite. At the top of the GHS, the STDS is composed of marble and metacarbonates plus subordinate calc-silicate gneiss and leucogranite intrusions at its base. Metamorphic grade of the STDS is poorly constrained, although index minerals record an upsection temperature decrease from clinopyroxene to biotite grade. The THS contains calcareous and pelitic metasedimentary rocks, metamorphosed at up to chlorite grade. In the Kali Gandaki Valley, the THS is deformed by the N-S striking Thakkhola Graben, which was active between midlate Miocene to Plio-Pleistocene times [*Colchen et al*., 1986; *Hurtado et al*., 2001; *Garzione et al*., 2003]. A geological field guide to the Kali Gandaki Valley has recently been published by *Carosi et al*. [2014].

2. Microstructure Analytical Methods

2.1. Optical Microscopy

Microstructural analysis of 104 samples was conducted via optical microscopy (see supporting information Data set S1 for sample list and *XZ* orientations) in the *XZ* plane of the kinematic reference frame (*X* points downdip, parallel to principal stretching and inferred transport direction, *Z* normal to foliation). We use the term "microstructure" to describe visible crystal structures (e.g., grain boundary morphology, subgrains, etc.). "Texture" describes a visible collection of microstructures that form distinct compositional structures (e.g., dynamic recrystallization textures). "Fabric" describes alignment of crystal axes or crystal shapes (e.g., crystallographic preferred orientation).

2.1.1. Deformation Microstructure Temperature Constraints

Specific microstructures provide an indication of deformation temperatures of quartz, calcite, dolomite, and feldspar. Deformation temperature constraints used in this study (Table 1) are summarized below.

Stipp et al. [2002] proposed a quartz deformation temperature thermometer based on dynamic recrystallization textures. The thermometer predicts that at geological strain rates of $\sim 10^{-12}$ to 10^{-14} s^{-1} the dominant quartz microstructures evolve from: (1) grain boundary bulging recrystallization (BLG; ~280–390°C) to (2) subgrain rotation recrystallization (SGR; ~420–490°C) to (3) grain boundary migration recrystallization (GBM; >530°C) [*Stipp et al*., 2002] (Table 1). Additionally, at higher temperature (>650°C), chessboard subgrain patterns are often observed in quartz, as a result of combined (c)<*a*> and {m}[*c*] slip [*Kruhl*, 1996] (Table 1).

Calcite twinning microstructures provide a low temperature (<400°C) deformation thermometer (Table 1). Analysis of naturally deformed limestones deformed at known temperature ranges revealed the dominance of thin twins (Type I) below 170°C and thick twins (Type II) above 200°C [*Burkhard*, 1993; *Ferrill et al*., 2004]. Above 250°C, the onset of dynamic recrystallization results in curved, tapered, and lensoid thick twins (Type III) that may become patchy and serrated (Type IV) with further recrystallization [*Burkhard*, 1993; *Ferrill et al*., 2004]. At higher temperatures and strains, dynamic recrystallization and twin migration work to remove twins [*Burkhard*, 1993; *Ferrill et al*., 2004]. The use of this thermometer is limited as calcite twins only form under low strain and recrystallization may occur at temperatures below 250°C [*Burkhard*, 1993; *Ferrill et al*., 2004]. An additional constraint is provided by the presence of dolomite twins, which form between 300 and 600°C [*Barber et al*., 1981] (Table 1).

Variations in feldspar recrystallization mechanisms provide some indication of deformation temperatures (Table 1). Recrystallization of feldspar occurs at temperatures of >450°C [*Tullis and Yund*, 1991; *Fitz Gerald and Stünitz*, 1993]. Correlation between naturally deformed feldspar with known temperature constraints and experimental deformation studies suggests that plagioclase develops BLG + SGR recrystallization textures between 450 and 650°C [*Tullis and Yund*, 1991; *Fitz Gerald and Stünitz*, 1993]. SGR + GBM recrystallization textures are more common above 550°C [*Fitz Gerald and Stünitz*, 1993; *Rosenberg and Stünitz*, 2003]. Diffusion creep becomes an important deformation mechanism in plagioclase at high strain/high

Table 1. Microstructures-Based Deformation Temperature Constraints

Mineral	Microstructure/Slip System	Temperature (°C)	Source
Quartz	Grain boundary bulging dynamic recrystallization (BLG)	270–390	*Stipp et al.* [2002]
	BLG-SGR transition	390–420	*Stipp et al.* [2002]
	Subgrain rotation dynamic recrystallization (SGR)	420–490	*Stipp et al.* [2002]
	SGR-GBM transition	490–530	*Stipp et al.* [2002]
	Grain boundary migration dynamic recrystallization (GBM)	>530	*Stipp et al.* [2002]
	Chessboard subgrains (CBS)	>650	*Kruhl* [1996]
	Quartz c-axis crossed girdle opening angle	Variable	*Kruhl*[1998], *Faleiros et al.* [2016]
	(c)<a> slip	300–400	*Baëta and Ashbee* [1969], *Mainprice et al.* [1986], *Schmid and Casey* [1986]
	Mixed <a> slip	400–500	*Baëta and Ashbee* [1969], *Mainprice et al.* [1986], *Schmid and Casey* [1986]
	{m}<a> slip	500–700	*Baëta and Ashbee* [1969], *Mainprice et al.* [1986], *Schmid and Casey* [1986]
	{m}[c] slip	>650	*Mainprice et al.* [1986]
Calcite	Type I twinning	<200	*Burkhard* [1993], *Ferrill et al.* [2004]
	Type II twinning	200–300	*Burkhard* [1993], *Ferrill et al.* [2004]
	Type III twinning	250–300	*Burkhard* [1993], *Ferrill et al.* [2004]
	Low Temperature' (LT) CPO configuration	<300–400	*Wenk et al.* [1987]
	High Temperature' (HT) CPO configuration	>300–400	*Wenk et al.* [1987]
	Calcite CPO strength > dolomite CPO strength	<550	*Delle Piane et al.* [2008]
	{r} slip	300–400	*De Bresser and Spiers* [1997]
	{f}<D2> slip	300–600	*De Bresser and Spiers* [1997]
	{f}<D3> slip	550–800	*De Bresser and Spiers* [1997]
	(c)<a> slip	500–800	*De Bresser and Spiers* [1997]
Dolomite	{f} twinning	300–600	*Barber et al.* [1981]
	Dolomite CPO strength > calcite CPO strength	>550	*Delle Piane et al.* [2008]
	Dolomite CPO strength = calcite CPO strength	500–600	*Delle Piane et al.* [2008]
	(c)<a> slip	<300	*Barber et al.* [1981]
	(c)<a> + {f} slip	300–600	*Barber et al.* [1981]
	{f} slip	>550	*Barber et al.* [1981]
Feldspar	BLG + SGR dynamic recrystallization	450–650	*Tullis and Yund* [1991], *Fitz Gerald and Stünitz* [1993], *Altenberger and Wilhelm* [2000]
	SGR + GBM dynamic recrystallization	>550	*Fitz Gerald and Stünitz* [1993], *Rosenberg and Stunitz* [2003]
	Diffusion creep associated strength drop	>600	*Altenberger and Wilhelm* [2000], *Rosenberg and Stunitz* [2003]

temperature conditions (600–700°C) and in K-feldspar at low differential stresses, and generally accommodates more strain than dislocation creep [*Schulmann et al.*, 1996; *Altenberger and Wilhelm*, 2000; *Rosenberg and Stünitz*, 2003; *Menegon et al.*, 2008].

2.2. SEM EBSD Analysis

Quartz, calcite, dolomite, and feldspar CPOs from 93 samples were analyzed via SEM EBSD. CPOs are graphically represented on pole figures (stereographic projections) contoured in multiples of uniform distribution (m.u.d.). For all pole figures, *X* plots to the right and represents the down plunge azimuth of the transport direction. All CPO-derived dextral shear sense indicators indicate a normal (hanging wall down) shear sense. All sinistral shear sense indicators indicate a reverse (hanging wall up) shear sense.

Previously documented relationships between quartz, calcite, dolomite, and feldspar CPO topologies and active crystal slip systems, shear sense, and strain geometry are summarized below. SEM EBSD analytical methods and additional figures of quartz, calcite, and dolomite slip systems are provided in supporting information Figures S1–S6.

2.2.1. Quartz CPO and Crystal Slip Systems

Quartz CPOs were measured from 93 samples along the entire lengths of both transects. Pole figures were constructed for <*a*>, {m}, (c), {r}, and {z} crystallographic axes, plotted on lower hemisphere equal-area projections (supporting information Data set S2).

During crystal plastic deformation, quartz can deform via <*a*> slip on the (c), {m}, {r}, and {z} planes (*r* and *z* planes collectively referred to as {r/z} planes) and also by {m}[*c*] slip (supporting information, Figure S1) [*Baëta and Ashbee*, 1969; *Linker et al.*, 1984; *Mainprice et al.*, 1986; *Schmid and Casey*, 1986]. Typically, (c)<*a*> slip (slip on the basal plane in one of three <*a*> directions) is common at lower greenschist facies conditions (~300–400°C, Table 1). Through middle greenschist to lower amphibolite facies conditions, {m}<*a*> and {r/z}<*a*> slip become increasingly active (~400–650°C, Table 1) [*Baëta and Ashbee*, 1969; *Mainprice et al.*, 1986; *Schmid and Casey*, 1986; *Lloyd et al.*, 1992; *Lloyd and Freeman*, 1994]. Above ~650–700°C, {m}[c] slip can occur [*Mainprice et al.*, 1986] (Table 1), although this may occur at lower temperatures in the presence of hydrolytic weakening [*Mainprice et al.*, 1986; *Morgan and Law*, 2004]. In the Annapurna-Dhaulagiri

samples, the strongest quartz CPO fabrics were consistently measured in quartzites. Well-developed quartz CPOs were also found in semipelitic and some gneissic samples, where quartz is a major constituent of the bulk mineral assemblage and forms load-bearing domains. *Barth et al*. [2010] provide a useful graphical summary of quartz CPO topology indicators for different slip systems and strain geometries.

Commonly, <*a*> slip occurs on a combination of (c), {m}, and {r/z} planes (Mixed <*a*> slip) to produce crossed girdle distributions of *c*-axes (viewed in the *XZ* kinematic plane, supporting information, Figure S2). Crossed girdle topology tends to indicate either a plane strain (Type I topology) or constrictional strain (Type II topology) geometry [*Lister*, 1977] (see supporting information Figure S2 for examples). Type II crossed girdles may also be indicative of "dry" high temperature (>650°C) dynamic recrystallization [*Morgan and Law*, 2004]. The symmetry of *c*-axis distributions with respect to sample coordinates (foliation and lineation) also provides a qualitative indicator of coaxial (symmetrical distribution) or noncoaxial (asymmetrical distribution) deformation [*Lister et al*., 1978; *Barth et al*., 2010] (supporting information Figure S2). CPO asymmetries produced by noncoaxial deformation can also indicate a shear sense [*Behrmann and Platt*, 1982] (supporting information Figure S2). The opening angles of quartz *c*-axis crossed girdle fabrics also provide indication of deformation temperatures [*Khrul*, 1998] (Table 1). Opening angles are determined from the radial angle between crossed girdle *skeletons* drawn on contoured *c*-axis pole figures (supporting information, Figure S3). Temperature estimates have a nominal uncertainty of ±50°C reflecting the potential variable influence of strain rate and hydrolytic weakening on opening angles [see *Law*, 2014 for a comprehensive review of quartz microstructure and opening angle thermometry].

2.2.2. Calcite and Dolomite CPO and Crystal Slip Systems

Calcite and dolomite pole figures were constructed from 42 samples for <*a*>, {m}, (c), {e}, {f}, and {r} crystallographic axes and the $<40\bar{4}1>$ twinning direction (referred to as <*D1*> from here on) and $<\bar{2}021>$ and $<10\bar{1}1>$ slip directions (referred to as <*D2*> and <*D3*>, respectively, from here on), plotted on lower hemisphere equal-area projections (supporting information Data set S3).

At low temperatures (<300°C), calcite deforms by twinning on the {e} plane in the <*D1*> direction [*Burkhard*, 1993; *De Bresser and Spiers*, 1997]. Dynamic recrystallization of calcite begins at ~250°C and dominates above 300–400°C [*Barber et al*., 1981; *Evans and Dunne*, 1991; *Weber et al*., 2001]. Above 300–400°C, {r}<*D2*> slip ± {r}<*a*> slip dominates. Subordinate {f}<*D2*> slip occurs between 300 and 600°C. Subordinate {f}<*D3*> and (c)<*a*> slip occur between ~550 and 800°C (supporting information, Figure S4) [*De Bresser and Spiers*, 1997; *Pieri et al*., 2001; *Bestmann and Prior*, 2003] (Table 1).

In dolomite, (c)<*a*> slip dominates below 300°C [*Barber et al*., 1981]. At intermediate temperatures (300-600°C, Table 1), twinning on the {f} plane in the <*D3*> direction occurs, with subordinate (c)<*a*> and {f}<*D2*> slip. At high temperatures (>550°C, Table 1), {f}<*D2*> slip dominates [*Barber et al*., 1981]. Slip on the {r}<*a*> system may also occur in dolomite at intermediate to high temperatures, but is always subordinate to other slip systems (supporting information, Figure S4) [*Barber et al*., 1981, 1994].

Dislocation glide within calcite and dolomite occurs in many directions and not all active slip systems produce CPOs parallel or perpendicular to the shear plane [*Trullenque et al*., 2006]. Coaxial and noncoaxial deformation of calcite may be determined from orthorhombic CPO symmetry and monoclinic CPO symmetry/asymmetry, respectively [*Wenk et al*., 1987; *Lafrance et al*., 1994; *Trullenque et al*., 2006]. It may also be possible to classify different calcite *c*- and *a*-axis CPO topologies as "Low Temperature" (typically greenschist) or "High Temperature" (typically amphibolite) fabrics, although exact temperature ranges are poorly constrained [*Wenk et al*., 1987; *Leiss and Molli*, 2003; *Trullenque et al*., 2006]. Examples of the described calcite CPOs are included in supporting information Figures S5 and S6.

The relationships between dolomite CPO topology, temperature, and strain geometry are less well constrained, although previous studies suggest a similar behavior to calcite [*Wenk and Shore*, 1975; *Delle Piane et al*., 2009]. Noncoaxial intracrystalline deformation (e.g., twinning) of both calcite and dolomite will rotate *c*-axis maxima *against* the shear direction, whilst dynamic recrystallization will rotate *c*-axis maxima *toward* the shear direction [*Lafrance et al*., 1994; *Leiss and Barber*, 1999; *Pieri et al*., 2001; *Trullenque et al*., 2006; *Delle Piane et al*., 2009]. Dolomite is stronger than calcite at low temperatures (<550°C) and weaker than calcite at high temperatures (>550°C) [*Delle Piane et al*., 2008]. Strain partitioning in calcite-dolomite aggregates is common and relative differences in CPO strength between these minerals may provide an additional temperature constraint [*Delle Piane et al*., 2008] (Table 1).

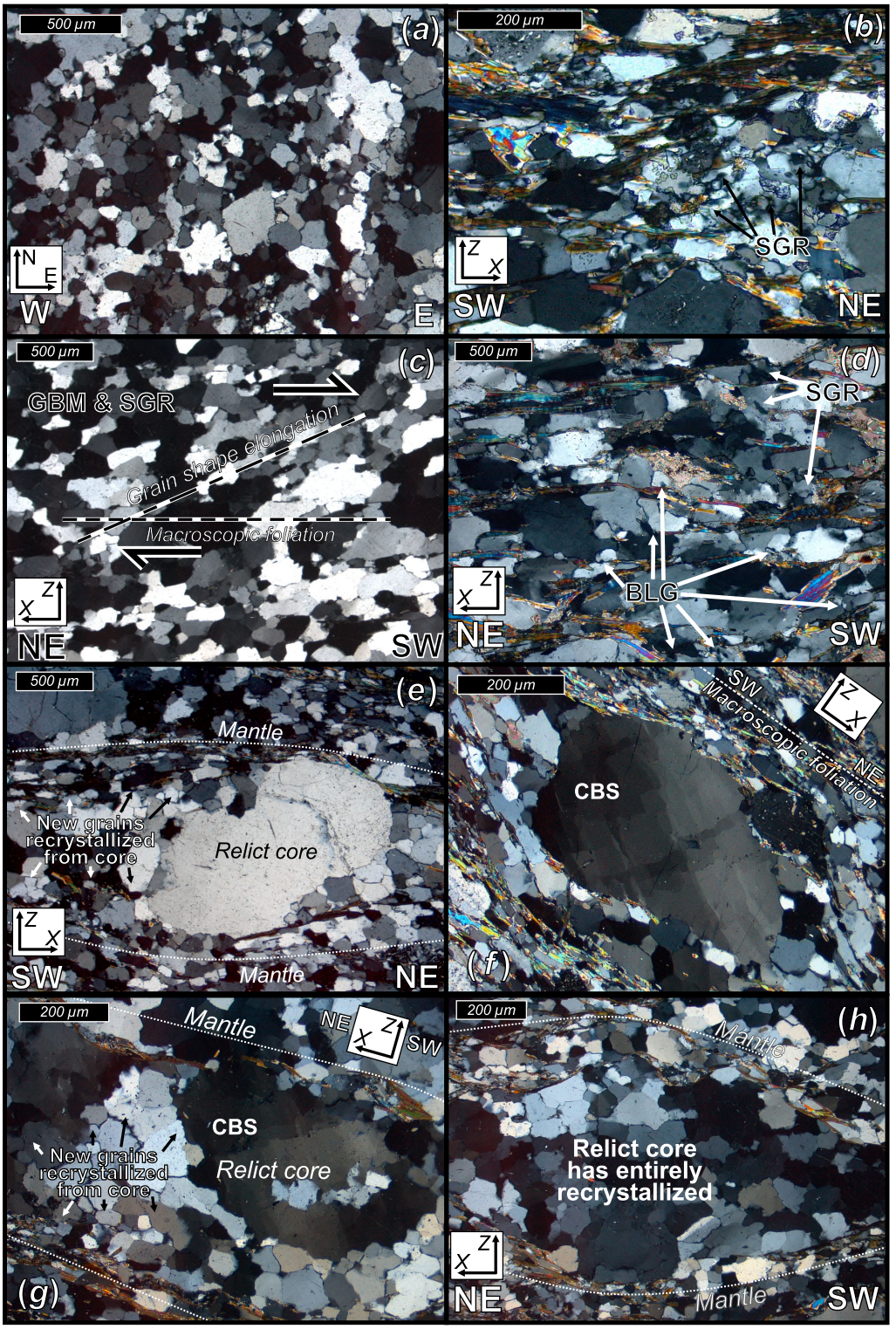

Figure 2. Quartz microstructures, (a) LHS, (b-g) LGHS. (a) Sample P12/084; (b) P13/053; (c) P12/030; (d) P13/049; (e) P12/078; (f) P13/052; (g) P13/051. Sample (XZ) and geographic coordinates indicated. See text for discussion.

2.2.3. Feldspar CPO and Crystal Slip Systems

Plagioclase and K-feldspar pole figures were constructed from 26 samples for the <100>, <010>, <001> directions, and for the (100), (010), and (001) poles to crystal planes (supporting information Data set S4).

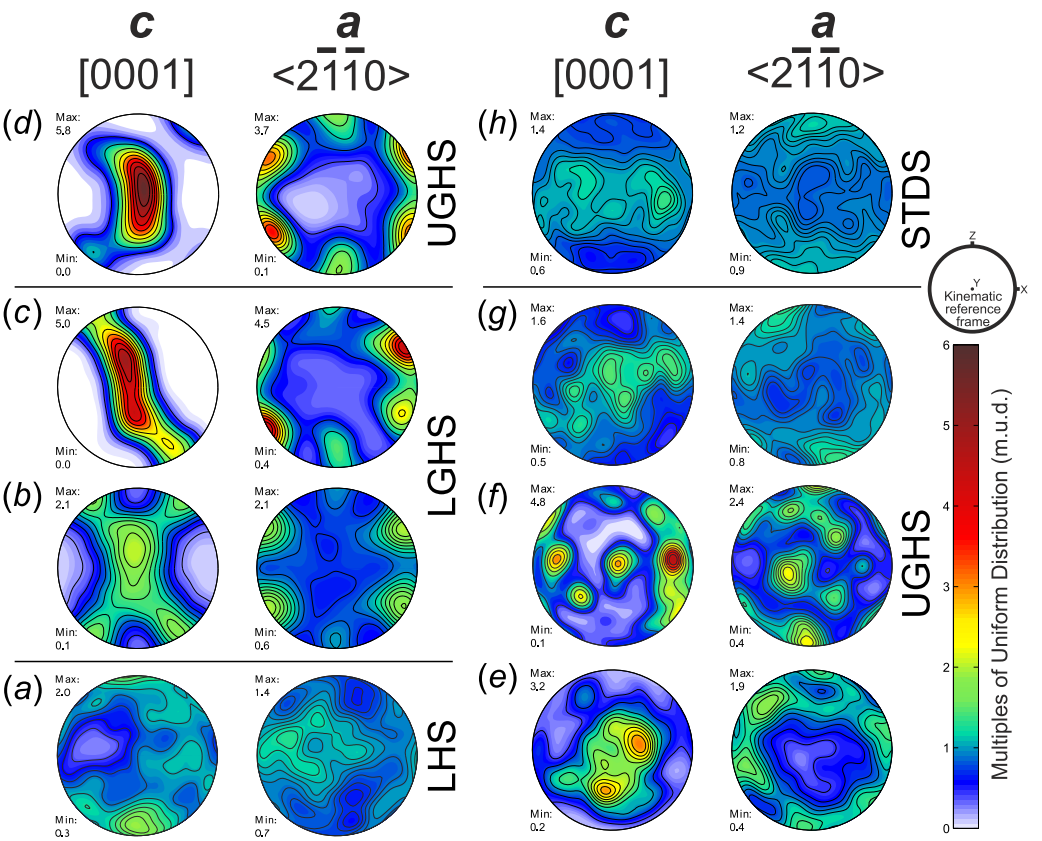

Figure 3. Selected quartz CPO fabrics. All plotted in XZ plane of kinematic reference frame with downdip direction of X to the right. Plotted with lower hemisphere equal area projection. (a) Sample P12/088—fabric indicates (c)<a> slip. (b) P13/062—mixed <a> slip, type I c-axis crossed girdle. (c) P12/030—mixed<a> slip with sinistral shear sense. (d) P12/061—{m}<a> slip, coaxial. (e) P13/045—{m}<a> slip. (f) P12/058—{m}[c] slip. (g) P13/040—{m}[c] slip with sinistral shear sense. (h) P12/045—rigid body rotation and/or preferential growth along the c-axis. Contoured for multiples of uniform distribution (m.u.d.). See text for discussion.

Pole figures were plotted on upper and lower hemisphere equal-area projections. Only feldspar CPOs from the UGHS and STDS, where temperatures were sufficient for significant intracrystalline deformation and recrystallization, are presented.

During intracrystalline deformation of plagioclase at medium to high grade conditions (>450°C), (010)<001> slip, and slip in the <110> direction on a plane anywhere between (001) and {111} is common, while (001)<100> and (010)<100> slip is also reported [*Olsen and Kohlstedt*, 1985; *Heidelbach et al*., 2000; *Stünitz et al*., 2003]. The mechanical behavior of K-feldspar is similar to plagioclase, and involves similar slip systems, the commonest being slip on the (010) plane in the <100>, <010>, <001>, and <101> directions [*Gandais and Willaime*, 1984; *Fitz Gerald and Stünitz*, 1993; *Menegon et al*., 2008]. Diffusion creep has been shown to weaken and/or modify CPO configurations due to anisotropic crystal growth rates of feldspar [*Bons and den Brok*, 2000; *Heidelbach et al*., 2000; *Menegon et al*., 2008; *Fukuda et al*., 2012].

3. Microstructural Analysis of the Annapurna-Dhaulagiri Himalaya

Deformation microstructures and CPO fabrics from each tectonostratigraphic unit are described and interpreted below. Selected CPOs are presented in Figures 3, 5, and 7 for reference. The majority of the fabrics discussed are to be found with their complete CPO data sets in supporting information Data sets S2–S4, as it is neither practical nor feasible to present all CPOs in a single figure. Corresponding deformation temperatures inferred from the observed microstructures and CPOs are discussed in section 4. A brief summary of field structures observed in each tectonostratigraphic unit is also given. Detailed field structural and petrological descriptions for the Modi Khola and Kali Gandaki transects have been reported by *Hodges et al*. [1996], *Godin* [2003], *Larson and Godin* [2009] *Carosi et al*. [2015], and *Parsons et al*. [2016b].

3.1. Lesser Himalayan Sequence (LHS)

The LHS is only weakly metamorphosed, with no field or microstructural evidence for internal penetrative shearing. Quartzites preserve original sedimentary structures such as cross bedding and ripple marks.

Quartz—Microstructures in the LHS typically define static recrystallization textures with euhedral crystal shapes and polygonal grain boundaries. Quartz deformation microstructures, including undulose extinction, deformation lamellae, fluid inclusion trails, and brittle fracturing are common. Partially annealed grain boundary bulging (BLG) dynamic recrystallization textures are sometimes observed (Figure 2a). The apparent degree of deformation is low compared to samples from the overlying GHS. Relict quartz grains (presumably detrital) have resisted recrystallization and often contain deformation kink bands.

In general, quartz CPOs from the LHS are weakly developed with poorly defined fabrics suggestive of (c)<*a*> slip (P12/088, Figure 3a). No discernible shear sense is recorded.

3.2. Lower Greater Himalayan Sequence (LGHS)

The LGHS is pervasively deformed throughout, and sheared quartz veins with a top-SW reverse shear sense are common. Top-SW shearing corresponds to development of the regional S3 foliation that transposes an earlier crenulation cleavage observed in the field in some metapelitic rocks [*Parsons et al*., 2016b]. The observed microstructures and CPO fabrics described below are associated with development of the regional S3 fabric.

Quartz—Partially annealed quartz deformation microstructures in quartzites and semipelites define an up-section transition from BLG and subgrain rotation (SGR) dynamic recrystallization textures (Unit A) to SGR and grain boundary migration (GBM) textures (Unit B and C) (Figures 2b–2d). In the lower LGHS, quartz porphyroclasts with larger grain size than surrounding matrix grains are observed (Figures 2e–2g). Where present, quartz SPOs indicate a top-SW shear sense (Figure 2c). In the Modi Khola transect, quartz porphyroclasts contain deformation bands and subordinate subgrains. In the Kali Gandaki transect, some quartz porphyroclasts display chessboard subgrain (CBS) textures (P13/051, P13/052, Figures 2f–2g). The edges of these porphyroclasts are often recrystallized to form core-mantle structures [e.g., *Passchier and Trouw*, 2005]. Recrystallized mantles are usually surrounded by an outer layer of mica that appears to define the original grain shape of the quartz core. In some cases, relict cores are entirely recrystallized, leaving a micaceous layer surrounding an aggregate of matrix-sized quartz grains (Figure 2h).

At the base of Unit A, quartz *c*-axis CPOs display a mix of type I (P13/062, Figure 3b) and type II (P12/080, P13/061, supporting information Data set S2) crossed-girdle fabrics, with weak asymmetry suggestive of noncoaxial, and possibly constrictional, sinistral shear (top-SW, reverse sense). In Unit B, quartz *c*-axis CPOs display strong, rotated, asymmetrical type I crossed girdles (P12/027, supporting information Data set S2) or single girdles (P12/030, Figure 3c), compatible with noncoaxial plane strain sinistral shear (top-SW). In these samples, a concentration of *c*-axis orientations parallel to the *Y* direction suggests a dominance of {m}<*a*> slip with minor contributions from (c)<*a*> and {r/z}<*a*> slip. In the Kali Gandaki transect, quartz CPOs from Unit C display weak (c)<*a*> slip compatible fabrics (P12/065, P13/049, supporting information Data set S2) with sinistral shear sense (top-SW).

A minority of samples in Unit A and C display *c*-axis girdles parallel to the *XY* plane (supporting information Data set S2—samples P13/054, P13/057, P12/066, see Figure 3h for an example from the STDS). The low-grade metamorphic indicator minerals in these samples indicate that these fabrics were not produced by high temperature {m}[*c*] slip (>650°C). Instead, preferential dissolution-precipitation growth of quartz parallel to the *c*-axis during phyllonitization is a more likely explanation [e.g., *Hippertt*, 1994; *Ihinger and Zink*, 2000].

Calcite and Dolomite—Metacarbonates and dolomitic marbles in Units B and C contain tabular calcite and dolomite grains with their long axes aligned subparallel to foliation. Grains show signs of grain boundary area reduction (GBAR) through both dynamic and static recrystallization (Figure 4). Calcite commonly displays type I and II twinning and occasionally preserves type III twins (Figure 4a). Dolomite grains are also twinned. In Unit C, deformed calcite and dolomite matrix grains sometimes surround isolated domains of quartz grains with BLG and SGR textures (Figure 4b).

Calcite and dolomite CPOs from Unit B and C are well defined (Figures 5a–5d). Where present in the same sample, calcite produces stronger CPO than dolomite. Rotated *c*-axis fabrics are common and suggest a

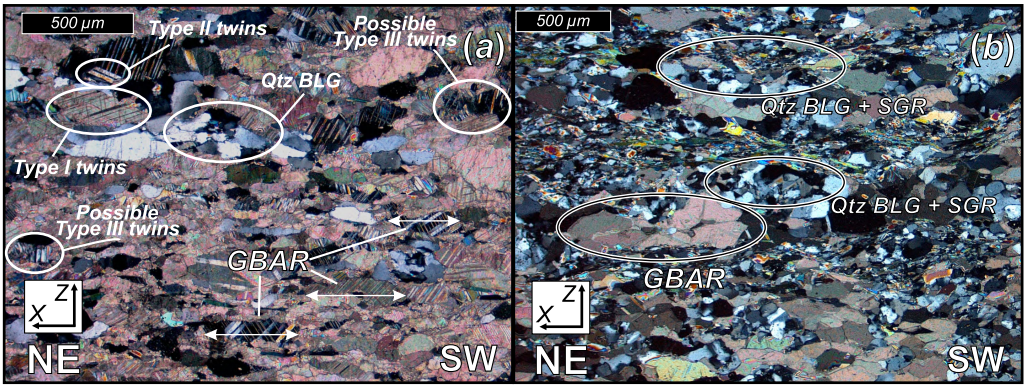

Figure 4. Metacarbonate/marble microstructures—LGHS. (a) Sample P12/026—Marble, (b) P12/068—Metacarbonate. Sample (XZ) and geographic coordinates indicated. See text for discussion.

sinistral shear sense (top-SW) (Figure 5c). The relative configuration of calcite crystallographic axes in these samples is compatible with activation of all slip systems, but only {r}<*a*> and (c)<*a*> slip could have occurred parallel to the flow plane. Calcite CPO configurations are similar to "Low Temperature" *c*-axis fabrics described by *Wenk et al*. [1987]. The recorded {f}, <*D2*> and <*D3*> fabrics are suggestive of either coaxial (e.g., P12/066, Figures 5a and 5b) or noncoaxial (e.g., P13/049, Figure 5c) deformation histories in individual samples. Typically, dolomite CPOs in the LGHS (e.g., P12/068, P12026, Figures 5a and 5d) are favorably oriented for (c)<*a*> and {r}<*a*> slip parallel to *X* ± subordinate {f}<*D2*> slip (P12/066, P12/063, supporting information Data set S3). A minority of dolomite CPOs have broad *c*-, *e*-, *r*-, *D2*-, and *D3*-axis maxima centered on the *Y* direction and poorly defined *a*-, *f*-, and *D1*-axis girdles parallel to the *XZ* plane (supporting information Data set S3). There are no previously published examples of this dolomite CPO (referred to here, as Type II dolomite CPO) and it is unclear what deformation mechanisms were responsible for its formation.

3.3. Upper Greater Himalayan Sequence (UGHS)

Field observations indicate that the UGHS is pervasively sheared throughout and contains evidence for both noncoaxial (e.g., shear folds) and coaxial (e.g., boudinage and isoclinal folding) deformation associated with formation of the regional, transpositional S3 foliation [*Parsons et al*., 2016b]. Migmatites are common throughout and preserve evidence for synmigmatitic deformation. A variety of high temperature deformation microstructures are observed across the UGHS. GBAR of all minerals is common throughout the UGHS. Tabular and elliptical grains orientated with long-axes parallel to foliation are common but give no indication of shear sense, except for samples from the base of the UGHS, which have well-defined top-WSW S-C fabrics and inclined SPOs (supporting information, Figure S7a). Garnet porphyroblasts do not display any sign of rotation (supporting information, Figure S7b). Where present, secondary muscovite has a random SPO indicating growth under static conditions. Partial melt textures are commonly observed. These include: (1) small (<10 μm) dihedral melt inclusions along feldspar and quartz grain boundaries (Figure 6f); (2) pore space psuedomorphs of feldspar and quartz (Figures 6f and supporting information S8a); (3) "string of beads" textures (Figure 6e); (4) euhedral feldspar neosomes surrounded by irregular shaped matrix grains of quartz, feldspar, and biotite (Figure 6a); (5) large (>1 mm) garnet and feldspar neosomes with smaller inclusions of quartz and biotite; and (6) large (>1 mm) euhedral apatite grains. These features are indicative of crystallization from a melt [e.g., *Holness and Sawyer*, 2008; *Sawyer*, 2008; *Holness et al*., 2011].

Quartz—Samples from the base of the UGHS display SGR and GBM quartz recrystallization textures. Quartz microstructures observed over the rest of the UGHS are dominated by GBM ± CBS recrystallization textures (Figures 6a–6h). Subordinate BLG + SGR quartz recrystallization textures are sometimes observed, particularly in samples from the Modi Khola transect (Figure 6g).

Quartz CPO fabrics (supporting information Data set S2) are poorly developed, perhaps reflecting the polymineralic composition of these rocks and the randomizing effects of static recrystallization and GBAR on CPO development. The structurally lowest *c*-axis CPO from Unit I in the Kali Gandaki transect defines a single girdle with remnants of a type I crossed girdle, compatible with {m}<*a*> slip plus minor (c)<*a*> and

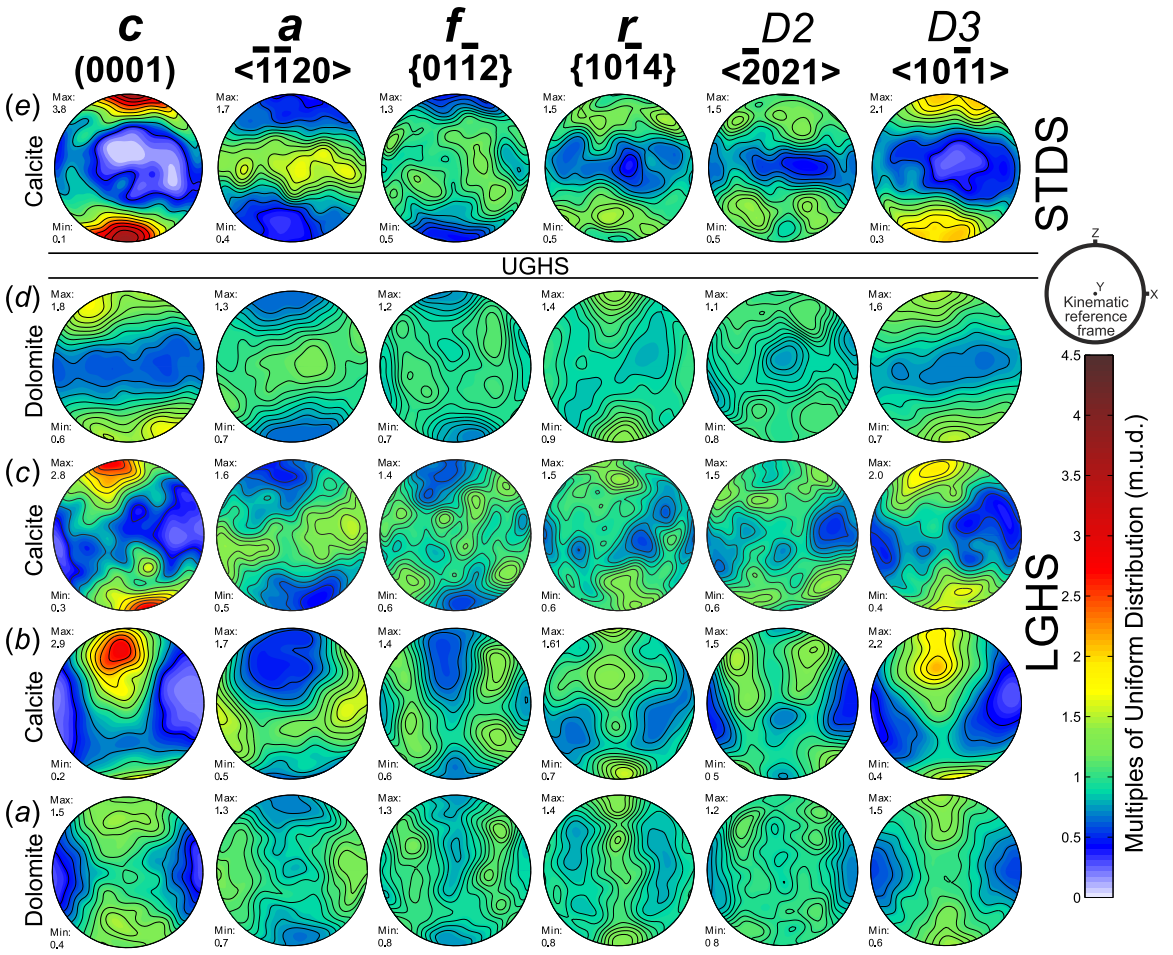

Figure 5. Selected calcite and dolomite CPO fabrics. All plotted in XZ plane of kinematic reference frame with downdip direction of X to the right. Plotted with lower hemisphere equal area projection. (a) Sample P12/068 dolomite—comparable to coaxial calcite CPO. (b) P12/066 calcite—comparable to "Low Temperature" coaxial fabric. (c) P13/049 calcite—comparable to "Low Temperature" noncoaxial fabrics with sinistral shear. (d) P12026 dolomite—comparable to noncoaxial fabric, with sinistral shear (e) P12/006 calcite—comparable to noncoaxial fabrics. Contoured for multiples of uniform distribution (m.u.d.). See text for discussion.

{r/z}<*a*> slip during plane strain noncoaxial sinistral shear (P13/046, supporting information Data set S2). Immediately above this, a quartzite sample yields a strong and well-defined type I *c*-axis crossed girdle distribution with no asymmetry and a point maxima parallel to the *Y* direction, suggestive of {m}<*a*> slip during plane strain coaxial deformation (P12/061, Figure 3d). In the Modi Khola transect, poorly defined quartz CPO fabrics from the base of Unit I are compatible with (c)<*a*> slip (P12/021 & P12/020, supporting information Data set S2). Across the rest of the UGHS, quartz CPO fabrics are poorly defined, but compatible with either {m}[*c*] slip (e.g., P12/058, P13/040, Figures 3f–3g) or {m}<*a*> slip (e.g., P13/045, Figure 3e). Most CPO fabrics are suggestive of coaxial plane strain, (i.e., *c*-axis *maxima* parallel to *X* direction, *a*-axis *maxima* parallel to *XZ* plane—P12/019, P12/054, P12/053; symmetrical type I *c*-axis crossed girdles—P12/013, P12/14 supporting information Data set S2), although some quartz CPOs suggest a degree of flattening strain (i.e., *c*-axis *girdle* parallel to *XY* plane, weak to no alignment of *a*-axis fabrics—P12/015, P12/058, P13/040—Figures 3f–3g and supporting information Data set S2) [e.g., *Barth et al*., 2010]. Rotation of *c*- and *a*-axes around *Y*, are rare, but suggest a minor amount of noncoaxial sinistral shear (top-to-the-SW/SE; e.g., P13/040, Figure 3g). In the Kali Gandaki transect, the uppermost quartz CPO from the footwall of the AD is compatible with (c)<*a*> slip and sinistral shear sense (top-WSW, P13/030, supporting information Data set S2).

Calcite—In the Kali Gandaki transect, calcite CPOs from calc-silicate gneisses in Unit II have poorly defined topologies, but have strong *c*-axis point maxima parallel to *Z* and *a*-axis girdles parallel to the *XY* plane (supporting information Data set S3). These CPO configurations are most suggestive of deformation via {c}<*a*> slip ± {f} slip.

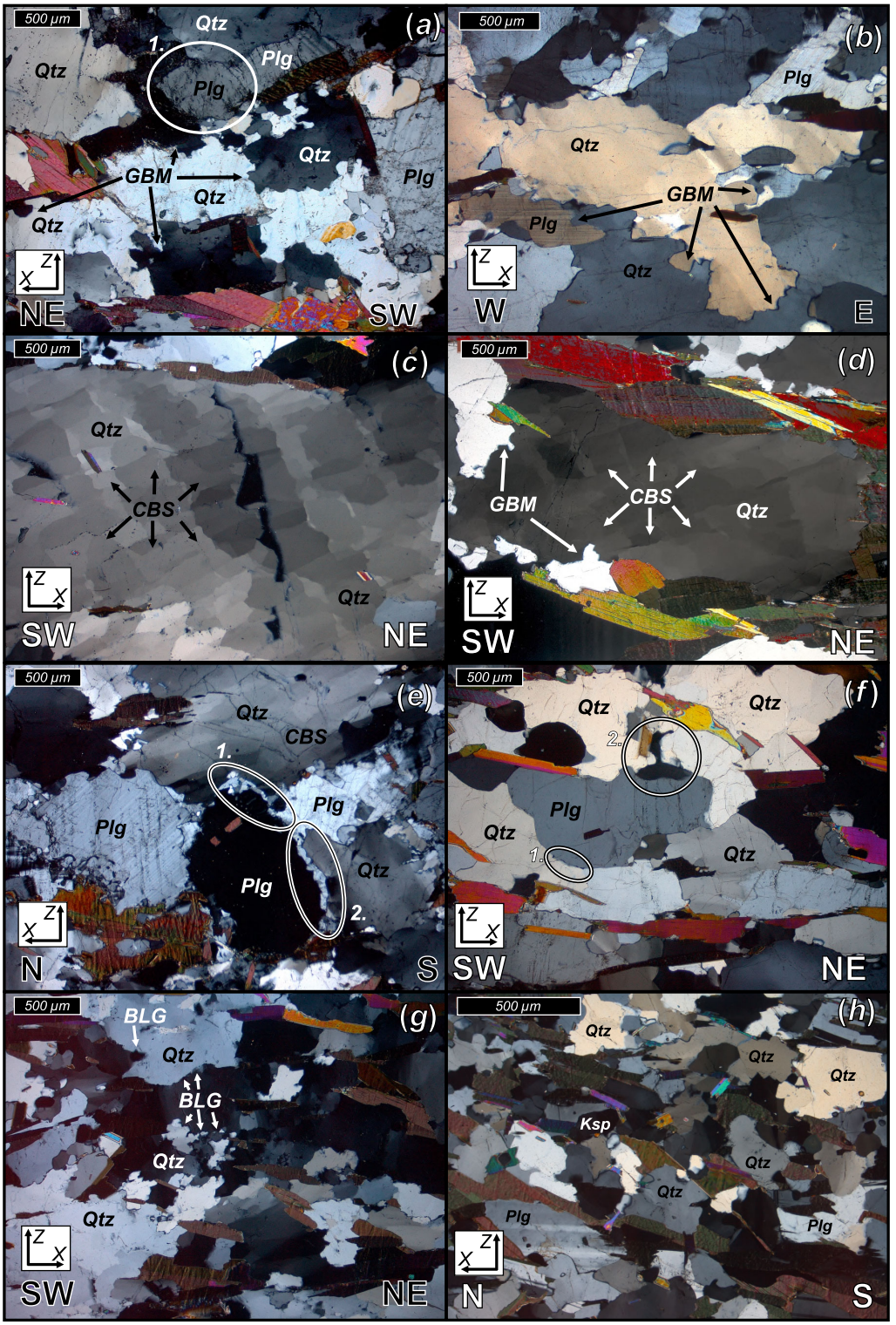

Figure 6. High temperature microstructures—UGHS. (a) Sample P12/015—white circle (a.) highlights euhedral plagioclase neosome that grew within/into melt space; (b) P12/049; (c) P12/017; (d) P12/058; (e) P12/012—circles (a.) and (b.) highlight "string of beads" partial melt textures; (f) P12/060—Circle (1) highlights possible melt inclusions along plagioclase grain boundary. Circle (2) highlights melt pore space pseudomorph of plagioclase; (g) P12/017; (h) P12/055. Sample (XZ) and geographic coordinates indicated. See text for discussion.

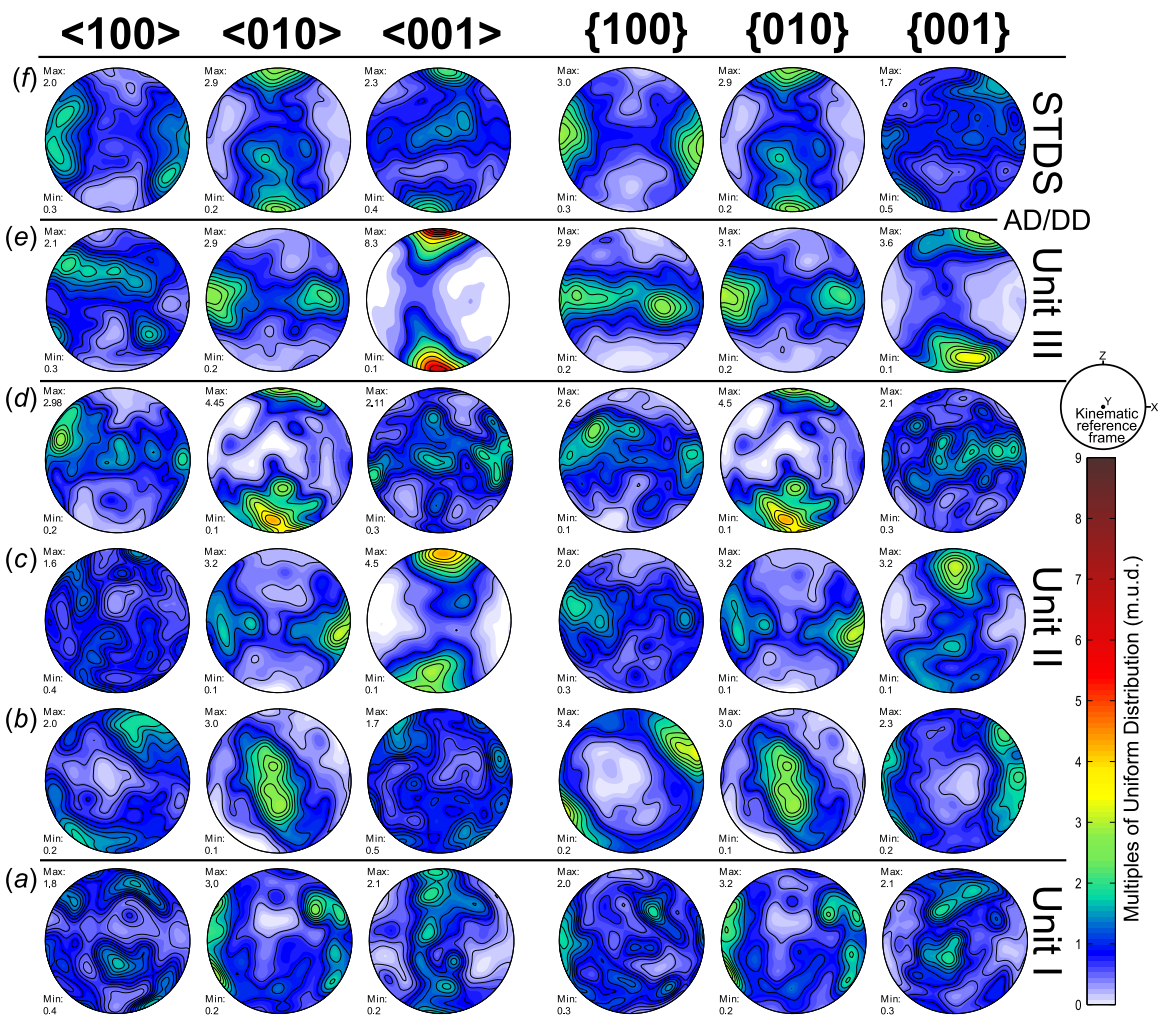

Figure 7. Selected feldspar CPOs. All plotted in XZ plane of kinematic reference frame with downdip direction of X to the right. Plotted with both upper and lower hemisphere equal area projection. (a) P12/059, Plagioclase; (b) P12/011, K-feldspar. (c) P12/054 Plagioclase; (d) P12/053, K-feldspar; (e) P13/032 Plagioclase; (f) P13/031,K-feldspar. Contoured for multiples of uniform distribution (m.u.d.). See text for discussion.

Feldspar—Feldspar grains across the UGHS display GBM and BLG recrystallization textures, diffusion creep textures, and growth and deformation twins (supporting information, Figure S8). Myrmkitic/granophyric feldspars are observed throughout.

Feldspar CPOs are generally weak and/or have no discernible fabric (supporting information Data set S4). In Unit I, a minority of CPOs may correspond to slip on (001) (P12/059, Figure 7a) and (010) (P13/044, supporting information Data set S4). In Unit II, K-feldspar CPOs are suggestive of slip on (010) (e.g., P12/053, Figure 7d), while strong plagioclase CPO may record (001)<110> slip (e.g., P12/054, Figure 7c). Unit III produces a minority of strong well-defined plagioclase and K-feldspar CPOs (e.g., P13/032; Figure 7e). These are favorably aligned for (001)<110> slip or (010)<001> and (010)<100> slip (P12/012, P12/049, P13/030, supporting information Data set S4). Some samples produce well defined nonrandom fabrics that do not correspond to known slip system configurations and may derive from diffusion creep controlled deformation (e.g., P12/011, Figure 7b).

Most feldspar CPOs record no definitive evidence for rotation due to noncoaxial deformation, except for the CPO for P13/032 (Figure 7e) that indicates a dextral (top-down-to-E) shear sense. Where feldspar CPOs are strong or have well-defined topology, <100> and <001> point maxima, respectively, parallel to the *X* and *Y* directions are common, and suggestive of plane strain deformation (P12/012, P12/059, P13/046, P13/044, supporting information Data set S4). In some samples, flow-plane (*XY*) parallel <100> or <001> girdles are also observed, particularly in the footwall and immediate hanging wall of the AD/DD (P12/053, P12/054,

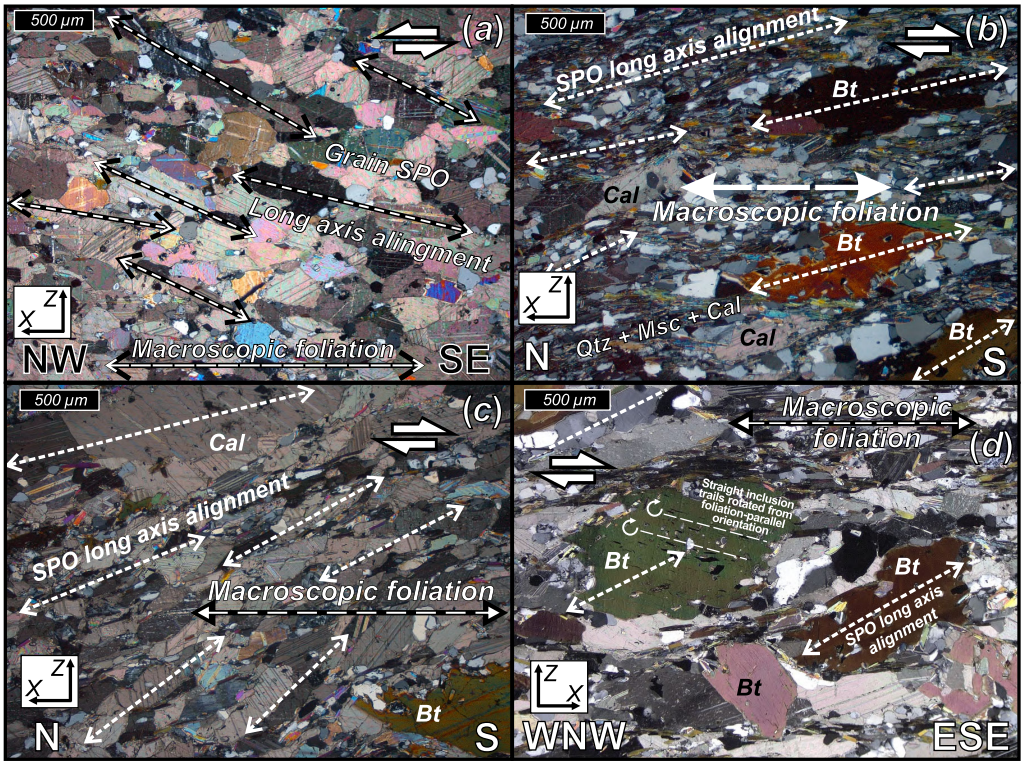

Figure 8. STDS shear sense indicators, Kali Gandaki. (a) Sample P13/026. (b-c) P13/008. (d) P12/044—Straight inclusion trails in biotite record a dextral rotation relative to the foliation. Sample (XZ) and geographic coordinates indicated. See text for discussion.

P13/032, Figures 3c–3e). These *XY* girdle fabrics may be indicative of a flattening-dominated strain (i.e., distributed dislocation glide within the *XY* plane).

3.4. South Tibetan Detachment System (STDS)

Indicators of pervasive, noncoaxial top-down-NE shearing are observed in the field throughout the STDS, and are associated with development of the regional transpositional S3 foliation [*Parsons et al*., 2016b]. In the Kali Gandaki valley, localized top-SW reverse sense shearing (S4) is sometimes observed overprinting the S3 foliation [*Parsons et al*., 2016b]. Most of the observed microstructures are associated with S3 foliation although some S4 microstructures are also observed.

Quartz—In the Modi Khola transect, quartz grain domains in the lower half of the STDS display GBM and CBS recrystallization textures and subordinate BLG recrystallization textures. In the Kali Gandaki transect, quartz domains are less deformed and display SGR and BLG textures.

Quartz CPOs (supporting information Data set S2) are weakly developed and commonly define *XY*-parallel *c*-axis maxima/girdles (Figure 3h). The lack of evidence for intracrystalline deformation of quartz suggests that these CPOs reflect mechanical rotation of quartz grains resulting in a shape-controlled CPO [e.g., *Stallard and Shelley*, 1995]. This probably requires preferential growth of quartz grains in the crystal [*c*] direction during or prior to rotation [*Ihinger and Zink*, 2000]. A single quartz CPO from an STDS leucogranite on the Modi Khola transect displays a {m}<*a*> slip CPO fabric with dextral shear (top-to-the-NE) asymmetry (P12/007, supporting information Data set S2).

Calcite and Dolomite—Elongate tabular grain shapes are displayed by calcite and dolomite across the STDS. Grain SPO long axes are typically inclined to the foliation (shear plane) and record either normal-sense (P13/026, P12044, Figure 8a; P13/005, supporting information Figure S9a) or reverse-sense shear (P13/008, Figures 8b and 8d; P13/006, supporting information Figure S9b). *Godin* [2003] and *Parsons et al.* [2016b] interpret reverse-sense shear indicators in the STDS as a younger fabric (S4) than normal-sense shear indicators (S3). Type I and II calcite twins are common. Type III calcite twinning is observed in samples from the base of the STDS. Where present, dolomite grains are also twinned. GBAR and partial annealing textures of

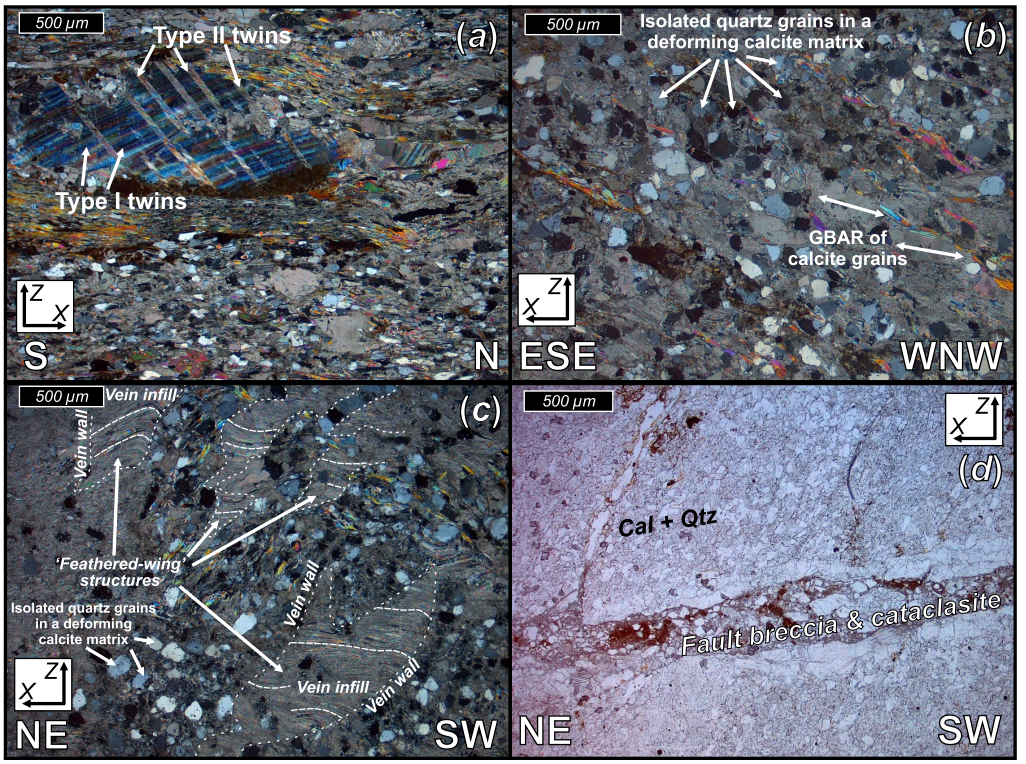

Figure 9. THS microstructures, Kali Gandaki. (a) Sample P12/037, (b) P12/038, (c) P12/039, (d) P12/039. Sample (XZ) and geographic coordinates indicated. See text for discussion.

calcite and dolomite are common. GBM and BLG textures are occasionally observed. In the top 40 m of the STDS, STD-related mylonitic calcite textures are observed.

Calcite CPO strength generally decreases up-section in the STDS (supporting information Data set S3). Calcite CPO topology varies and fabrics suggestive of both noncoaxial (P12/006, Figure 5e) and coaxial (P13/031, supporting information Data set S3) deformation are locally recorded. These calcite CPOs are favorably orientated for {*r*}<*a*> and {c}<*a*> slip in the *XY* plane parallel to *X*. Well-formed {f} girdles and <*D2*> and <*D3*> small circle girdles and point maxima suggest that {r}<*D2*> and {f} slip may have also occurred. Samples with calcite-dolomite aggregates from the middle and top of the STDS all have dolomite fabrics that are stronger than calcite fabrics. The strongest dolomite CPOs are found at the very top of the STDS (P13/005, P13/006, supporting information Data set S3). These dolomite CPOs are favorably orientated for (c)<*a*> and {r}<*a*> slip in the *XY* plane and {f} slip in the *XZ* plane. A minority of calcite and dolomite CPOs display clockwise or anticlockwise rotation about the *Y* axis, respectively, suggestive of dextral (top-to-the-ESE; P12/044, supporting information Data set S3) and sinistral (top-to-the-WSW; P12/043, supporting information Data set S3) noncoaxial shear.

Feldspar—At the base of the STDS, plagioclase grains displays GBM + GBAR textures and sometimes contain subgrains. Myrmekite and perthite textures indicate that dissolution-precipitation was a significant deformation mechanism. Plagioclase CPOs from the base of the STDS (P12/007, P13/031 supporting information Data set S4) are compatible with (001)<110>slip, while K-feldspar CPOs are favorably orientated for (010)<100> and/or (001)<100> slip (e.g., P13/031, Figure 7f). Rotated plagioclase CPO fabrics in the hanging wall of the AD suggest dextral (top-down-to-E) shear (P13/031, supporting information Data set S4). Feldspar grains in the upper portion of the STDS are largely undeformed with no indication of dynamic recrystallization.

Other minerals—At the base of the STDS in the Kali Gandaki transect, hornblende porphyroblasts have core-mantle structures indicating a normal-sense top-to-the-E shear. Phlogopite and biotite grains are observed across the STDS and typically form a spaced cleavage between bands of calcite and quartz that define the

regional foliation (supporting information, Figure S9c). The upper portion of the STDS in the Kali Gandaki valley contains biotite porphyroblasts, of which some are chloritized. In the middle of the STDS, these porphyroblasts are equant and euhedral and form core-mantle structures with either top-to-the-S (reverse, Figure 8d) or top-to-the-ESE (normal, Figure 8c) shear senses. Toward the top of the STDS, biotite porphyroblasts become increasingly flattened, boudinaged, and rotated parallel to foliation (supporting information, Figure S9d).

3.5. Tethyan Himalayan Sequence (THS)

The THS is deformed by km-scale folds and thrusts associated with development of an S2 axial planar foliation that deforms an earlier bedding-subparallel S1 foliation. Toward the base of the THS, STDS-parallel S3 foliation transposes S1 and S2. Top-SW contractional S4 foliation and a E-W extensional S5 cleavage are observed locally throughout the THS [*Godin*, 2003; *Parsons et al*., 2016a]. Observed microstructures are generally associated with formation of the regional S2 foliation, with the exception of samples from the base of the THS that are dominated by S3 associated deformation.

Quartz—In the THS, quartz grains are generally undeformed and commonly observed as isolated, circular grains with no internal deformation, surrounded by a deformed matrix of calcite and/or mica (Figures 9a and 9b). Quartz CPO fabrics are very weak to random (supporting information Data set S2). *XY*-parallel *c*-axis point maxima/girdle fabrics are common (e.g., P12/041, P12/038, supporting information Data set S2) and most likely result from shape-controlled mechanical rotation [e.g *Stallard and Shelley*, 1995] and/or preferential dissolution-precipitation growth in the direction of the crystal *c*-axis [e.g., *Hippertt*, 1994; *Ihinger and Zink*, 2000].

Calcite and Dolomite—In the lower 1.5 km of the THS, calcite, and dolomite microstructures record both brittle and crystal plastic deformation. Grains are small, anhedral, and commonly display type I and occasionally type II twins, with signs of grain growth around undeformed quartz (Figures 9a and 9b). Foliation-cross-cutting fractures and fractured calcite grains are common (Figure 9d). "Feathered wing-like" calcite amalgamations are also observed that appear to have formed as vein-calcite precipitating rapidly into voids and fractures that formed during deformation (Figure 9c). These microstructures are likely to have formed during motion on the STD. Above this structural level, microstructures are dominated by a local foliation, which is commonly defined by spaced cleavage between mica and carbonate bands.

Calcite and dolomite CPOs (supporting information Data set S2) are weak, with the exception of the lower and uppermost samples (P12/041, P12/033, supporting information Data set S2). Discernible fabrics are comparable to "Low Temperature" CPOs, favorably orientated for $\{c\}\langle a\rangle \pm \{r\}\langle a\rangle$ slip parallel to *X* in the *XZ* plane. At the base of the THS, calcite CPOs suggest reverse sense sinistral shear (top-to-the-W; P12/041, supporting information Data set S3) that correlates with observed SPOs. Structurally above this, calcite and dolomite CPOs (P12/039, supporting information Data set S3) from the footwall to a low angle fault (150/26 NE) suggest normal sense dextral shear. The strong calcite CPO from the top of the Kali Gandaki transect (P12/033, supporting information Data set S3) may relate to top-east normal-sense shearing on the Dangardzong fault, which flanks the western margin of the Thakkhola Graben [*Hurtado et al*., 2001].

4. Thermal Profile of the Annapurna-Dhaulagiri Himalaya

We now constrain deformation temperature ranges (Table 1) for the GHS and bounding units using: (a) the recorded microstructures identified via optical microscopy and, (b) the EBSD-derived CPO fabrics and their inferred active crystal slip systems. Quartz *c*-axis fabric opening angle thermometry, using data from universal-stage (U-stage) and EBSD CPO analyses of 25 samples, provides additional constraints on deformation temperatures (supporting information, Figures S10–S12 and Table S1). Opening angle derived deformation temperatures were estimated using the thermometer of *Kruhl* [1998]. Temperature estimates determined from the newly published opening angle thermometer of *Faleiros et al*. [2016] are within error of those derived from the *Kruhl* [1998] thermometer (supporting information, Table S1).

Deformation microstructures developed through crystal plastic creep evolve to attain steady state equilibrium textures that reflect PT conditions (among other factors) under which they formed [*Nicolas and Poirier*, 1976; *Means*, 1981]. If crystal plastic deformation ceased prior to reaching stead state, then preserved microstructures may also contain relict textures/fabrics which pertain to earlier PT conditions [*Passchier and*

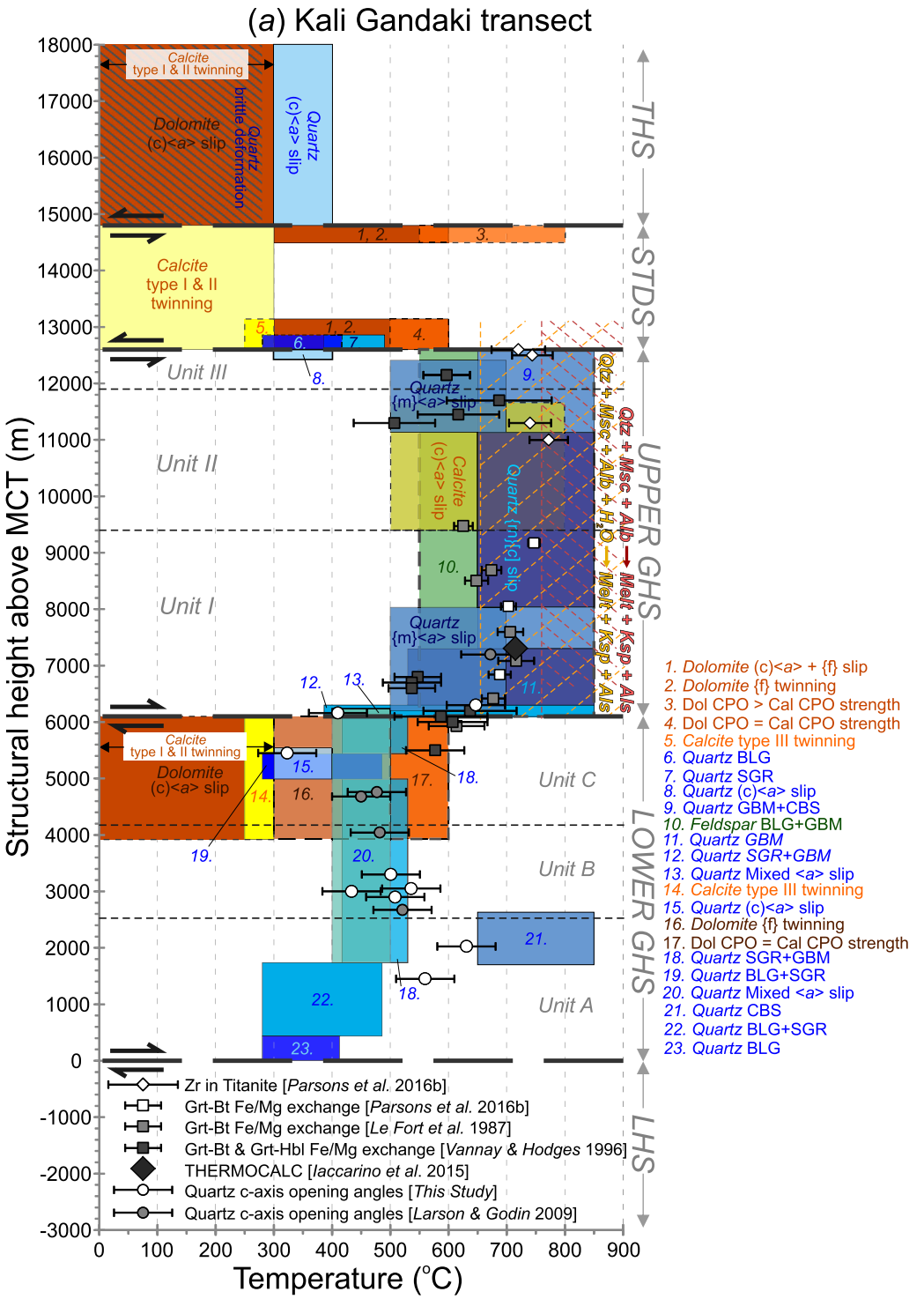

Figure 10. Deformation temperature profile for (*a*) Kali Gandaki and (*b*) Modi Khola transects. Colored boxes correspond to a specific deformation microstructure or active slip system. Size and position of each box represents the temperature range of microstructure/slip system (horizontal-axis) and observed structural position above the MCT (vertical-axis). Temperature constraints are presented in Table 1. Fields of dashed red lines and dashed orange lines, respectively, indicate temperature range of fluid-absent and fluid-present muscovite dehydration melt reactions [*White et al.*, 2001] at peak pressure (11 kbar—Kali Gandaki transect, 12 kbar—Modi Khola Transect) [*Parsons et al.*, 2016b *and references therein*]. Data points superimposed on colored boxes correspond to temperature estimates derived from quartz c-axis fabric opening angle thermometry, (white and grey circles—*this study*, *Larson and Godin* [2009]), RSCM thermometry (grey triangles—*Beyssac et al.* [2004]), garnet-biotite, garnet-ilmenite, and garnet-hornblende cation-exchange thermometry (white, grey, and black squares—*Le Fort* [1975]; *Kaneko* [1995]; *Vannay and Hodges* [1995]; *Martin et al.* [2010]; *Corrie and Kohn* [2011]; *Parsons et al.* [2016b]), Zr-in-titanite thermometry (white and grey diamonds—*Corrie and Kohn* [2011]; *Parsons et al.* [2016b]) and THERMOCALC multiphase equilibria results [*Iaccarino et al.*, 2015].

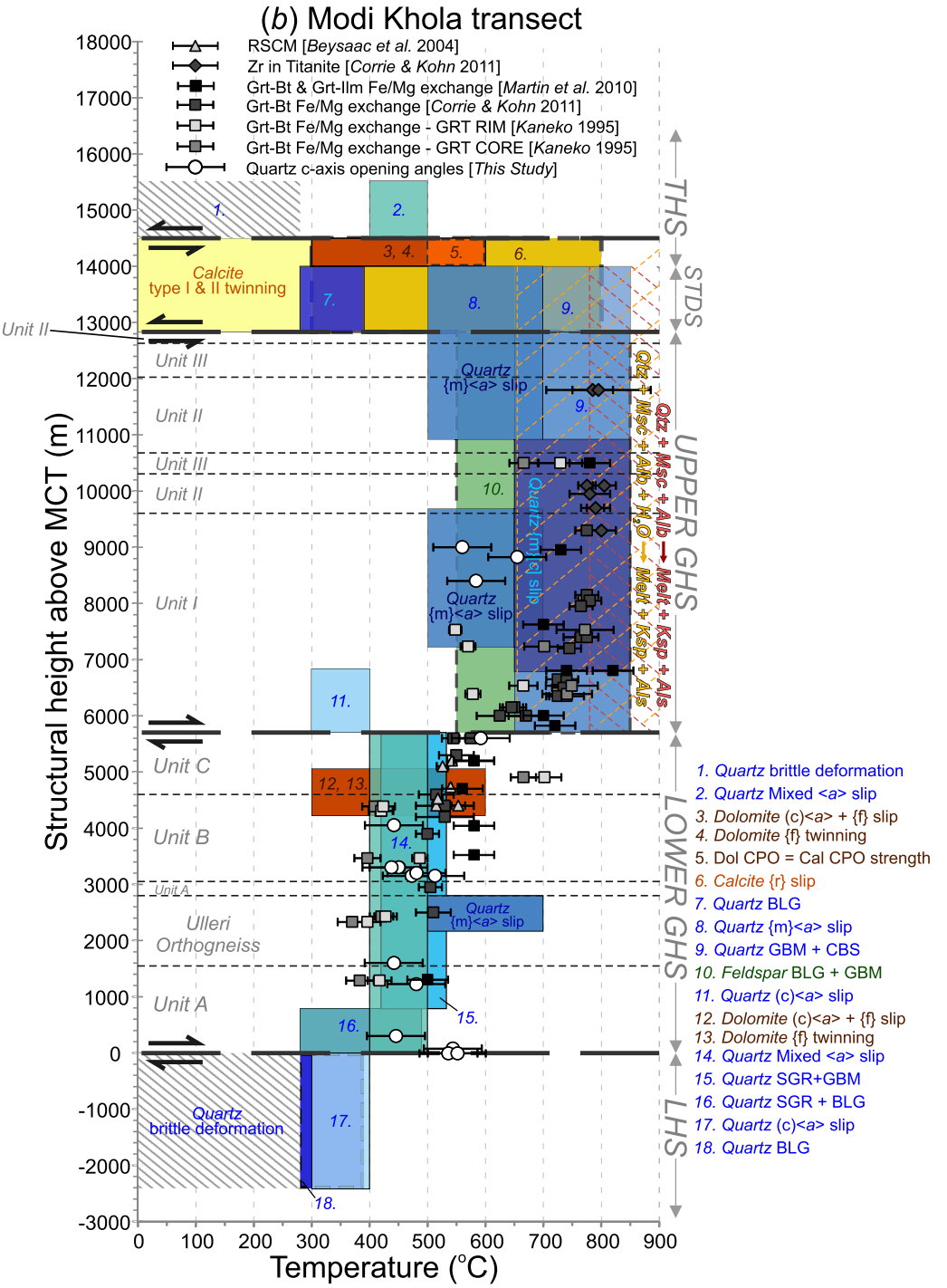

Figure 10. (continued)

Trouw, 2005]. However, during progressive deformation through dynamic PT space, recrystallization mechanisms will work to remove earlier fabrics, such that the preserved microstructures may reflect only the *final* PT conditions under which they formed [*Knipe and Law*, 1987]. This phenomenon is common in exhumed metamorphic rocks that often preserve deformation microstructures indicative of pressures and temperatures that are lower than petrology and mineral chemistry-derived peak PT estimates [e.g., *Larson and Godin*, 2009; *Wallis et al.*, 2014]. In such situations, preserved microstructures are more likely to correlate

with PT estimates associated with the retrograde part of the P-T-time path. In order to take this possibility in to account, deformation temperature constraints derived from our microstructural and CPO data are combined with previously published petrology-derived peak and retrograde temperature estimates. These combined data sets are used to construct tectonostratigraphic deformation temperature profiles for the GHS of the Kali Gandaki and Modi Khola transects (Figure 10).

4.1. LHS

In the LHS (Figure 10b), brittle and low temperature ductile quartz microstructures (BLG) and quartz (c)<*a*> slip fabrics indicate a deformation temperature range of <280°C to 300–400°C.

4.2. LGHS

In the LGHS, quartz microstructures record deformation temperatures of ~280–490°C (BLG + SGR) in the lowermost 1–2 km and ~420–530°C (SGR + GBM) above this structural level (Figure 10). Quartz slip systems typically indicate deformation temperatures of 400–500°C (Mixed <*a*> slip). Dolomite twinning and slip system activity is suggestive of deformation at 300–600°C in Units B and C (Figure 10). In the Kali Gandaki transect (Figure 10a), Unit C contains lower temperature quartz, calcite, and dolomite microstructures, while CPO patterns and inferred slip systems are indicative of a wider range of deformation temperatures (quartz: 280–530°C; calcite and dolomite: >250°C and <300°C).

Quartz *c*-axis opening angles from the Modi Khola transect (Figure 10b) indicate deformation temperatures of 500–600°C in the immediate hanging wall of the MCT. Above this level, opening angle temperature estimates increase up-section from ~400–500°C (Unit A), to ~550–650°C (Unit C). In the Kali Gandaki transect (Figure 10a), quartz *c*-axis opening angles from both this study and *Larson and Godin* [2009] record an up-section *decrease* in temperatures from ~500–650°C, to 300–400°C (discussed below).

High temperature microstructures and CPO fabrics are preserved in the Ulleri Gneiss in the Modi Khola valley (500–700°C, {m}<*a*> slip) and at the same structural level above the MCT in Units A and B (>650°C, CBS textures) in the Kali Gandaki valley. CBS textures are preserved in large relict cores of core-mantle structures and are recrystallized to smaller matrix-sized grains at their margins. This suggests that high temperature deformation occurred early in the rocks' deformation history prior to development of lower temperature fabrics and textures in the surrounding matrix grains. Given the lack of field and microstructural evidence for localized deformation at this structural level, we speculate that these high temperature (500–700°C) quartz microstructures and CPO fabrics may correspond to Palaeoproterozoic emplacement of the Ulleri gneiss magmatic protolith [*Pêcher and Le Fort*, 1977; *DeCelles et al*., 2000], rather than being produced during Himalayan age out-of-sequence thrusting within the LGHS.

Previously published garnet-biotite (GARB), garnet-ilmenite, and Raman Spectroscopy of Carbonaceous Material (RSCM) thermometry from the LGHS in the Annapurna-Dhaulagiri region record peak temperatures of ~450–600°C that increase up-section [*Le Fort et al*. 1987; *Beyssac et al*., 2004; *Martin et al*., 2010; *Corrie and Kohn*, 2011]. Garnet rim GARB thermometry records retrograde temperatures of ~400–450°C [*Kaneko*, 1995].

4.3. UGHS

High temperature deformation is recorded across the UGHS (Figure 10) both by quartz microstructures (>650°C, GBM + CBS) and slip systems (500–700°C, {m}<*a*> slip; >650°C, {m}[*c*] slip) and by feldspar microstructures (>550°C). Active calcite slip systems in Unit II of the Kali Gandaki transect (>500°C, (c)<*a*> slip) support this interpretation. Lower temperature quartz microstructures and slip systems (300–530°C) are localized in the immediate hanging wall of the CT. Additionally, quartz (c)<*a*> slip (~300–400°C) is recorded in the immediate footwall of the AD in the Kali Gandaki transect (Figure 10a). Temperatures indicated by quartz *c*-axis fabric opening angles increase up-section from 360 to 460°C in the immediate hanging wall of the CT to ~500–700°C across the rest of Unit I [this study, plus *Larson and Godin*, 2009].

Previously published garnet-biotite, garnet-ilmenite, and garnet-hornblende cation-exchange and Zr-in-titanite thermometry and multiphase equilibria modeling from the UGHS in the Annapurna-Dhaulagiri region indicate that peak temperatures of metamorphism did not exceed ~850°C [*Le Fort et al*., 1987; *Kaneko*, 1995; *Martin et al*., 2010; *Corrie and Kohn*, 2011; *Kohn and Corrie*, 2011; *Iaccarino et al*., 2015; *Parsons et al*., 2016b]. Peak temperatures of metamorphism increase up-section (Figure 10) from ~600–750°C at the

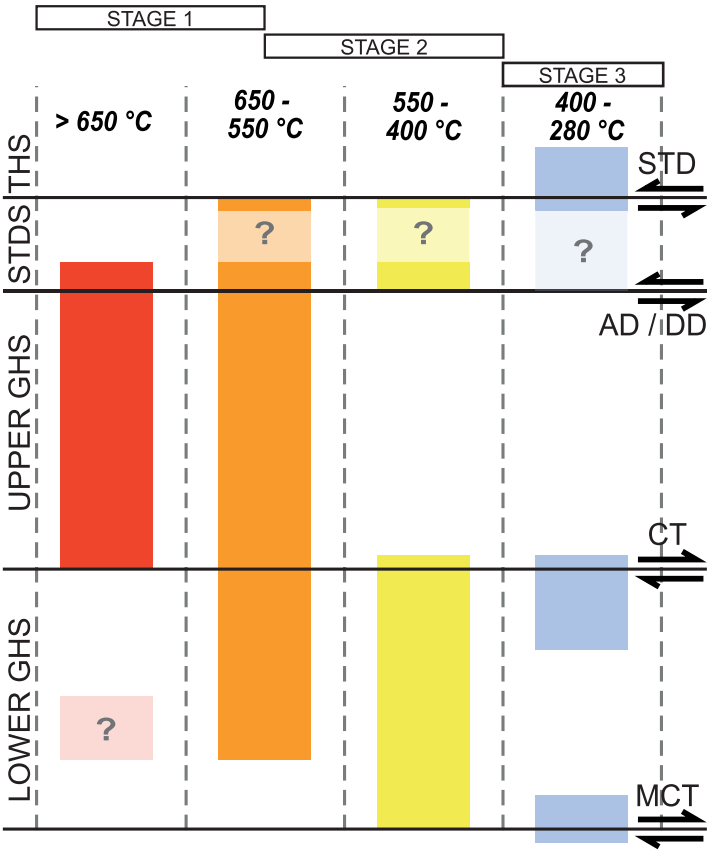

Figure 11. Summary of deformation temperatures recorded in the GHS and THS. Individual columns correspond to specific different deformation temperature ranges. Colored bars indicate locus of deformation across the structural transects for each temperature range. Pale colored bars with question marks denote sections where deformation temperatures are poorly constrained and/or do not fit regional trend. *AD, Annapurna Detachment; CT, Chomrong Thrust; DD, Deurali Detachment.*

base of Unit I to ~650–800°C at 0.5–1.5 km above the CT and 700–850°C across the rest of the UGHS [*Le Fort et al.*, 1987; *Kaneko*, 1995; *Martin et al.*, 2010; *Corrie and Kohn*, 2011; *Iaccarino et al.*, 2015; *Parsons et al.*, 2016b]. Additionally, in the Modi Khola transect garnet rim temperatures of 550–600°C and ~700°C [*Kaneko*, 1995] are recorded from the lower and middle portions of the UGHS, respectively (Figure 10b).

4.4. STDS

Deformation temperatures in the STDS are poorly constrained. The base of the STDS contains deformed leucogranites, which together with quartz, calcite, and dolomite microstructures and CPO fabrics, indicate deformation temperature ranges of >650°C, and ~300–600°C (Figure 10). Calcite twins across the whole of the STDS record low strain deformation at <300°C. No useful deformation temperature indicators were found in the central portion of the STDS. At the top of the STDS, intermediate deformation temperatures (300–600°C) are recorded by dolomite microstructures and CPO patterns.

In the Kali Gandaki transect (Figure 10a), Zr-in-titanite thermometry records metamorphism at temperatures of 730 ± 60°C in the immediate hanging wall of the AD [*Parsons et al.*, 2016b].

4.5. THS

Quartz, calcite, and dolomite microstructures and inferred crystal slip systems indicate low to intermediate deformation temperatures in the THS (<300–400°C).

5. Thermokinematic Evolution of the Annapurna-Dhaulagiri Himalaya

Our study provides a record of deformation from 104 samples collected from an 18 km thick structural section through the entire GHS and the upper and lower bounding THS and LHS. Observed microstructures and CPO fabrics indicate deformation temperatures ranging from >700°C to <280°C (Figure 10; summarized in Figure 11). Previous studies in the Annapurna-Dhaulagiri region have focused mostly on determining petrology-derived *peak metamorphism* PT conditions from the UGHS [e.g., *Martin et al.* 2010; *Corrie and Kohn*, 2011]. Combining these previously published data with our record of microstructure-derived deformation temperatures provides a more complete thermokinematic record of deformation for the entire GHS, plus the upper and lower portions of the LHS and THS, respectively (summarized in Figure 11). The preserved syntectonic partial melt textures together with the overprinting relationships of lower temperature on higher temperature microstructures indicate that these profiles record progressive deformation on a

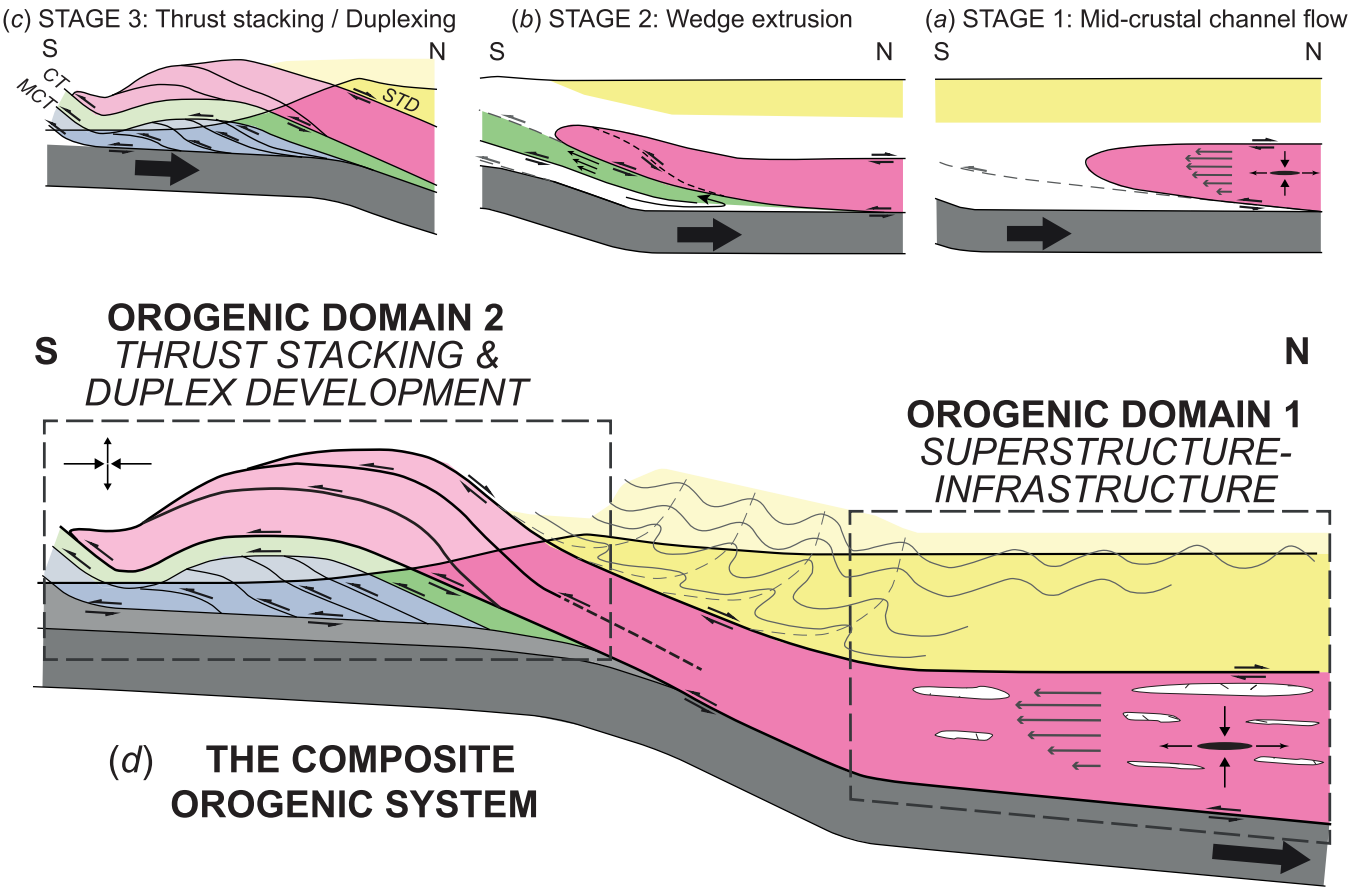

Figure 12. Model for progressive development of a Composite Orogenic System in the Annapurna-Dhaulagiri region with schematic transport-parallel cross sections illustrating the different stages of formation. Pink—UGHS +STDS; Yellow—THS; Green—LGHS; Blue—LHS; Grey—Indian lower crust. (a) Stage 1: Mid crustal channel flow of the UGHS beneath the Tibetan Plateau. (b) Stage 2: Wedge extrusion of rigid, cooler, foreland-positioned UGHS (potentially still driven by channel flow in hinterland beneath Tibetan Plateau), facilitated by pervasive noncoaxial shearing in the LGHS (green). Thrusting within UGHS may also occur. (c) Stage 3: Duplexing/thrust stacking of LHS beneath the foreland-positioned LGHS facilitates exhumation of the GHS. Not to scale. (d) The Composite Orogenic System. Schematic cross-sectional model of the present-day Himalayan orogen comprising multiple "orogenic domains." See text for discussion.

retrograde path from peak conditions during early-stage mid-crustal extrusion to late-stage upper crustal exhumation (Figure 11).

Traced up-section, deformation temperature profiles for both transects generally mimic the well-documented inverted metamorphic profiles (*with the exception of LGHS Unit C, Kali Gandaki transect—see below*) that are documented from the lower portions of GHS-equivalent sections throughout the central and eastern Himalaya [e.g., *Le Fort*, 1975; *Caddick et al.*, 2007; *Mottram et al.*, 2014]. Gradational changes in our deformation temperature record (Figure 10) help identify specific tectonic units with distinct deformation histories that are potentially similar to other parts of the central and eastern Himalaya. As such, the thermokinematic evolution of the GHS in the Annapurna-Dhaulagiri Himalaya can be divided into three distinct stages (Figures 12a–12c), defined by the observed distribution and migration of deformation through evolving temperature regimes. As indicated by the distribution of specific temperature-dependent microstructures in our deformation temperature profiles (Figure 10; summarized in Figure 11), these stages operated at different crustal positions within the progressively evolving Himalayan orogen.

5.1. Stage 1: Midcrustal Flow (>700°C, 11–14 kbar to 550–650°C, 7–8 kbar)

The earliest deformation stage (Figure 12a) is characterized by penetrative shearing throughout the UGHS and base of the STDS, which occurred at, and close to, peak temperature and pressure conditions (~700–850°C, 11–14 kbar) [*Parsons et al.*, 2016b and references therein] (Figure 11). Field observations confirm that deformation took place contemporaneously with partial melting. Microstructural partial melt textures (Figures 6e–6f) indicate that the UGHS preserves deformation from peak temperature conditions and that

partial melts cooled and crystallized slowly from peak temperatures. Kinematic data determined from microstructures and CPO fabrics mostly record coaxial deformation. Noncoaxial deformation dominates at the margins of the UGHS. Additionally, quartz and feldspar CPOs record components of plane strain and flattening strain across the UGHS. Thermochronological constraints indicate that high temperature kyanite-grade metamorphism initiated at ~48–43 Ma and continued to at least 28 Ma [*Carosi et al*., 2015; *Iaccarino et al*., 2015; *Larson and Cottle*; 2015]. Partial melting initiated at 41–36 Ma and continued to 22–18.5 Ma [*Hodges et al*., 1996; *Godin et al*., 2001; *Carosi et al*., 2015; *Larson and Cottle*, 2015]. These thermokinematic constraints are readily explained by an initial phase (Stage 1) of midcrustal channel flow of the UGHS [e.g., *Jamieson et al*., 2004; *Grujic*, 2006; *Rosenberg et al*., 2007; *Jamieson et al*., 2011; *Parsons et al*., 2016b] between 48 Ma and 18.5 Ma (Figure 12a).

Assuming that deformation temperatures indicated by the observed microstructures reflect conditions during the last stages of ductile deformation [e.g., *Knipe and Law*, 1987], quartz deformation temperatures indicate that pervasive ductile deformation/flow in the UGHS ended at ~550–650°C (Figure 11). These temperature conditions correlate with garnet rim GARB thermometry [*Kaneko*, 1995] and multiphase equilibria modeling [*Iaccarino et al*., 2015] that yield temperatures of metamorphism of 650–670°C at 7–8 kbar in Unit I of the Kali Gandaki transect during retrogression at 25–18 Ma. These data are comparable to adjacent peak PT estimates from the underlying LGHS [*Le Fort et al*., 1987; *Martin et al*., 2010; *Corrie and Kohn*, 2011]. Additionally, these P-T-time constraints also correlate with both the youngest crystallization ages of partial melts and minimum ages of pervasive top-SW and top-NE/E shearing in the UGHS at 22–18 Ma [*Nazarchuk*, 1993; *Hodges et al*., 1996; *Godin et al*., 2001; *Corrie and Khon*, 2011], and the minimum temperature for fluid-present muscovite dehydration melting at 7–8 kbar [*White et al*., 2001].

We interpret these P-T-time data to record cooling and mechanical strengthening of the UGHS. It is likely that the accompanying increase in viscosity associated with this cooling and strengthening would have hindered the ability of the UGHS to deform as a midcrustal channel flow and may have been responsible for the eventual cessation of flow, as suggest by *Parsons et al*. [2016b], between 25 and 18 Ma at ~550–650°C, 7–8 kbar. As such, these PT conditions may corresponds to the threshold viscosity (i.e., maximum viscosity) for midcrustal channel flow in the Annapurna-Dhaulagiri Himalaya [e.g., *Grujic*, 2006; *Rosenberg et al*., 2007; *Jamieson et al*., 2011] and signify the transformation of the UGHS from a pervasive extrusive flow ("Active channel") to rigid block behavior ("Channel plug") [*Beaumont et al*., 2001; *Parsons et al*., 2016b]. The proposed PT conditions for this transformation reflect the *minimum* PT conditions for ductile deformation within the UGHS. These PT conditions are equivalent to *peak* PT estimates from the underlying LGHS. We propose that the cooling and strengthening of the UGHS, which we interpret to reflect the cessation of channel flow, was accompanied by migration of deformation from the now strengthened UGHS into mechanically weaker rock units of the underlying LGHS, and possibly into the overlying STDS. This migration of deformation was necessary to facilitate exhumation of the rigid UGHS, which could no longer deform internally via pervasive ductile flow, and defines the transition from Stage 1 to Stage 2 (Figure 12b).

5.2. Stage 2: Rigid Wedge Extrusion and Exhumation (~400–600°C, <7–9 kbar)

Stage 2 deformation (Figure 12b) occurred at deformation temperatures of ~400–600°C and corresponds to exhumation of the UGHS as a rigid block, facilitated by ductile shearing in the underlying LGHS (Figure 11). This is supported by kinematic indicators such as SPO and S-C fabrics and rotated asymmetric CPOs, which indicate a dominance of noncoaxial plane strain deformation in the LGHS. During this stage, penetrative deformation was pervasively distributed throughout the LGHS, which behaved as a crustal scale (~5 km thick) shear zone. The overlying UGHS deformed only at its margins (Figure 12b). The downsection distribution of deformation temperatures in the LGHS shows no correlation with the location of lithological boundaries. Furthermore, metamorphic indicator minerals provide no indication of distinct metamorphic discontinuities between units (with the exception of Unit C, see below), and no obvious unit-bounding shear zones were observed in the field. Consequently, deformation within the LGHS is most comparable to a broad zone of pervasive ductile shearing rather than localized deformation between discrete thrust slices. These structural processes are comparable to those invoked by rigid wedge extrusion models [e.g., *Burchfiel and Royden*, 1985] and models for the exhumation of a solid "channel flow plug" [e.g., *Beaumont et al*., 2004]. Peak pressure estimates (~7–9 kbar) from the LGHS suggest Stage 2 initiated at a maximum depth of ~21–27 km [*Le Fort et al*., 1987; *Martin et al*., 2010; *Corrie and Kohn*, 2011]. Approximately uniform $^{40}Ar/^{39}Ar$ muscovite cooling ages suggest the UGHS exhumed through the muscovite closure temperature for Ar loss

(380–450°C) [*Harrison et al*., 2009] at 16–13 Ma as a single coherent block [*Vannay and Hodges*, 1996; *Godin et al*., 2001; *Martin et al*., 2015]. Out-of-sequence thrusting within the UGHS (Kalopani and Modi Khola shear zones) [*Hodges et al*., 1996; *Vannay and Hodges*, 1996] and localized shortening within the STDS [*Godin*, 2003; *Parsons et al*., 2016b] occurred sometime after the cessation of top-NE/E motion on the AD/DD (22–18 Ma) [*Hodges et al*., 1996; *Godin et al*., 2001] and before wholesale exhumation of the UGHS (16–13 Ma) [*Vannay and Hodges*, 1996; *Parsons et al*., 2016b]. A single $^{40}Ar/^{39}Ar$ muscovite crystallization age of 17 Ma from the THS in the Kali Gandaki valley has been interpreted as a record of out-of-sequence thrusting [*Godin et al*., 2001; *Parsons et al*., 2016b]. Therefore, Stage 2 initiated sometime after 22–18 Ma and was active at 16–13 Ma.

5.3. Stage 3: Duplexing/Thrust Stacking (<280–400°C)

Stage 3 records localization of brittle-ductile deformation on the MCT, CT, and within Unit C of the LGHS (Figure 12c) at 400°C to <280°C (Figure 11). Metapelitic rocks are common at these structural positions and display well-defined top-SW S-C fabrics and high concentrations of sheared quartz and/or calcite veins. Phyllonitization and chloritization of these rocks are prevalent.

In Unit C of the LGHS in the Kali Gandaki transect (Figure 10a), deformation temperatures derived from quartz fabric opening angles and microstructures are lower than those derived from the same thermometers in the underlying LGHS units (Figure 10a). We suggest that the dominance of metapelitic rocks within Unit C may have promoted localization of late-stage deformation during exhumation at lower temperatures, after cessation of deformation in the relatively stronger quartzite and marble layers of Units B and A. Within Unit C, well-defined top-SW S-C fabrics and sheared calcite veins observed in the field, and chloritization and sericitization of biotite microlithons and feldspar porphyroclasts observed in thin section, are compatible with this interpretation.

Localized deformation within Unit C (Figure 10) coincides with the proposed location of the Munsiari thrust [*Kohn*, 2008; *Corrie and Kohn*, 2011]. This thrust was originally described in the Kumaun Himalaya in NW India [*Valdiya*, 1980] but has since been extrapolated along strike into the central Himalaya [e.g., *Srivastava and Mitra*, 1994; *Khanal et al*., 2015; *Robinson and Martin*, 2014]. We found no discrete thrust plane to attribute to the Munsiari thrust; however, localized low temperature deformation in Unit C may be associated with such a structure. Low temperature quartz microstructures and slip systems in the immediate footwall and hanging wall of the AD in the Kali Gandaki transect (Figure 10a), may also record localized shortening in the STDS during Stages 2 and/or 3 [*Godin*, 2003; *Parsons et al*., 2016b].

Localization of strain during this final stage of ductile deformation is likely to reflect a positive feedback between initial partitioning of strain in to mechanically weaker rock layers, followed by localized strain softening (e.g., through phyllonitization) [*Wallis et al*., 2015] and further strain partitioning. This feedback is strengthened if deformation occurs during decreasing temperatures, as strain will naturally migrate in to, and accumulate within, mechanically weaker rock layers. These processes result in a series of rigid thrust sheets separated by narrow, weak shear zones, comparable to processes associated with duplexing and thrust stacking [e.g., *Srivastava and Mitra*, 1994; *Robinson et al*., 2006; *He et al*., 2014]. The lower temperature, upper crustal nature of this deformation suggests that this final stage (Figure 12c) occurred synchronously with development of the Lesser Himalayan Duplex that initiated at 14–11 Ma [e.g., *DeCelles et al*., 2001; *Paudel and Arita*, 2006; *Robinson and Martin*, 2014]. A single $^{40}Ar/^{39}Ar$ muscovite cooling age of 7 Ma from the LGHS [*Martin et al*., 2015] suggests localized low temperature deformation (<380–450°C) within the LGHS and on the MCT probably occurred during or after this time.

These findings highlight a clear distinction between the kinematic evolution of the LGHS and UGHS. Following cessation of crustal flow in the UGHS, the LGHS formed a crustal-scale shear zone that facilitated rigid body translation of the overlying UGHS as a single coherent block during exhumation starting at temperatures and pressures of ~550–650°C and 7–8 kbar. The evolution of deformation through Stages 2 and 3 is comparable to findings from similar studies elsewhere in the Himalaya that record a downsection decrease in deformation temperatures in LGHS-equivalent stratigraphy [*Bouchez and Pêcher*, 1981; *Yakymchuk and Godin*, 2012; *Law et al*., 2013; *Larson and Cottle*, 2014]. It is possible that Stages 2 and 3 were active simultaneously at different structural positions within the orogen, with Stage 2 at a deeper hinterland position and Stage 3 at a shallower foreland position. The downsection decrease in minimum deformation temperatures within the LGHS suggests that the LGHS thickened as the MCT migrated downsection during exhumation

due to accretion/underplating of underlying material [e.g., *Montomoli et al*., 2015; *Mottram et al*., 2015; *Larson et al*., 2015]. Based on these findings, we consider the whole of the LGHS to be synonymous to the Main Central Thrust Zone (MCTZ) [e.g., *Grasemann et al*., 1999; *Mottram et al*., 2015; *Larson et al*., 2015].

5.4. The Composite Orogenic System

The tectonic processes described in this study (channel flow, wedge extrusion, duplexing/thrust stacking) have been individually presented by other authors as possible models for Himalayan orogenesis. Some of these models have been presented as mutually exclusive end-members [e.g., *Robinson et al*., 2006; *Kohn*, 2008; *Carosi et al*., 2010] with supporting evidence for any one process used as evidence against the occurrence of the other two. This dichotomy may be overcome if the rheological boundary conditions that govern the structural development of an orogen are considered to vary through time and space [e.g., *Jamieson and Beaumont*, 2013; *Cottle et al*., 2015]. Application of this concept indicates that a variety of orogenic processes, commonly perceived as mutually exclusive "end-member" processes may operate within distinct Orogenic Domains that form modular components to a single Composite Orogenic System (Figure 12d) [e.g., *Larson et al*., 2010; *Larson and Cottle*, 2014; *Cottle et al*., 2015; *Searle*, 2015].

The data presented here provide insight into the thermo-kinematic evolution of the GHS in the Annapurna-Dhaulagiri Himalaya. Three orogenic stages defined by distinct tectonic processes are identified (Figures 12a–12c), corresponding to migration of the GHS through distinct Orogenic Domains (Figure 12d) within the Himalayan Composite Orogenic System. Stage 1 (Figure 12a) describes the midcrustal evolution of the GHS under conditions indicative of channel flow (Orogenic Domain 1). This domain typifies the Superstructure-Infrastructure Association, [e.g., *Williams et al*., 2006; *Jamieson and Beaumont*, 2013], in which the rheological contrast between the partially molten midcrust (Infrastructure—UGHS) and the cold strong upper crust (Superstructure—THS) results in a mechanical decoupling (STDS) between the two rheologic units. Midcrustal deformation in Orogenic Domain 1 is characterized by vertical shortening and horizontal stretching during pervasive plane strain and general flattening shear [e.g., *Law et al*., 2004, 2011; *Jessup et al*., 2006; *Larson and Godin*, 2009; *Parsons et al*., 2016b].

Stage 3 (Figure 12c) describes the upper crustal evolution of the GHS, defined by thrust stacking and duplex development (Orogenic Domain 2). Deformation in Orogenic Domain 2 is characterized by horizontal shortening and vertical thickening during localized simple shear (plane strain). Stage 2 (wedge extrusion and exhumation, Figure 12b) represents a transition stage between Domains 1 and 2 and reflects transport-parallel rigid body translation of the UGHS through the brittle-ductile transition zone (Figure 12d).

An important implication of the Composite Orogenic System is that multiple Orogenic Domains, with contrasting tectonic processes and rheologies, may be active at the same time. Comparison with numerical simulations also suggests that Orogenic Domains linked by a transitional stage (i.e., Stage 2) may become dynamically coupled, such that a change in boundary conditions in one domain will affect deformation processes in the other [e.g., *Jamieson and Beaumont*, 2013].

Such concepts are similar to recently published composite tectonic models for the Himalayan orogeny, which involve elements of two or more of the "end-member" models [e.g. *Larson et al*., 2010; *Spencer et al*., 2012; *Jamieson and Beaumont*, 2013; *Mukherjee*, 2013; *Wang et al*., 2013; *He et al*., 2014; *Larson and Cottle*, 2014; *Ambrose et al*., 2015; *Cottel et al*., 2015]. Applying these concepts to previous studies that argued for the prevalence of one tectonic process over another [e.g., *Robinson et al*., 2006; *Kohn*, 2008] suggests that these apparently contradictory studies may actually record deformation from different orogenic domains. Our findings demonstrate that channel flow, wedge extrusion, and duplexing/thrust stacking processes are not incompatible but rather, reflect spatial and temporal variations in rheological boundary conditions within a Composite Orogenic System [*Larson et al*., 2010; *Jamieson and Beaumont*, 2013; *Cottle et al*., 2015; *Searle*, 2015].

6. Conclusions

Microstructural analysis has been conducted on 104 samples from two orogen-perpendicular transects through the metamorphic core (GHS) and bounding units (LHS, THS) of the Annapurna-Dhaulagiri Himalaya, central Nepal. SEM EBSD analyses have been performed on 93 of these samples. Results record progressive deformation of the GHS along a retrograde path from early-stage high temperature ductile deformation

and partial melting at peak metamorphic conditions (≥650°C) to low temperature ductile (400–280°C) and brittle (<280°C) deformation during exhumation.

The UGHS contains microstructures indicative of pervasive high temperature ductile deformation in the presence of partial melt (550°C to >700°C). Dislocation creep of quartz and feldspar plus diffusion creep of feldspar is evident. Deformation is predominantly by coaxial plane strain, with a minor component of general flattening shear. Pervasive deformation within the UGHS did not occur below temperatures of ~550°C. Microstructures and CPO fabrics in the LGHS and STDS record intermediate to low temperature (280–650°C) noncoaxial, plane strain, ductile deformation. Dislocation creep of calcite, dolomite, and quartz is evident. Lower temperature microstructures and CPO fabrics (280–400°C) are observed in the footwall and hanging wall of the CT and MCT, respectively (LGHS), and in the footwall of the STD (STDS). The LHS and THS record low temperature ductile (280–400°C) and brittle (<280°C) deformation.

New deformation temperature profiles for the Annapurna-Dhaulagiri Himalaya reveal three distinct deformation stages during extrusion and exhumation of the GHS from peak conditions: Stage 1 (>700°C to 550–650°C)—channel flow of the UGHS; Stage 2 (600–400°C)—rigid wedge extrusion of the UGHS via pervasive shearing in the underlying LGHS; Stage 3 (<400°C)—duplexing/thrust stacking in the LGHS and LHS via localized thrust faulting. This kinematic evolution is best explained in terms of a Composite Orogenic System, which describes the migration of the GHS through distinct Orogenic Domains with contrasting rheological conditions. High temperature midcrustal channel flow of the UGHS is confined to Orogenic Domain 1, located in the hinterland of the orogenic system, and characterized by vertical shortening and horizontal stretching during pervasive plane strain and general flattening shear (Stage 1). Low temperature exhumation of the GHS occurs in Orogenic Domain 2, located towards the foreland, and characterized by localized thrusting during horizontal shortening and vertical thickening of the Himalayan Duplex (Stage 3). Stage 2 records rigid body translation of the UGHS from Domain 1 to Domain 2. These Orogenic Domains are located at different crustal positions in the Composite Orogenic System and may be active at the same time. This highlights the importance of considering the rheological, as well as the temporal, evolution of mountain belts.

Previously, these orogenic processes (channel flow, wedge extrusion, duplexing/thrust stacking) have been presented as mutually exclusive models. Our findings show that at least in the case of the Annapurna-Dhaulagiri Himalaya, channel flow, wedge extrusion, and duplexing/thrust stacking all played an integral part in the evolution of the Himalaya. Importantly, this study demonstrates that these processes need not be thought of as incompatible end-members if orogenesis is considered in terms of an evolving rheology.

Acknowledgments

We thank Brad Hacker and an anonymous reviewer for their constructive suggestions that helped to improve this work. We also thank G Cubed editor Cin-Ty Lee and an anonymous associate editor who oversaw the review and revision process. Suka Ghale, Basan Sherpa, and their Nepalese colleagues are thanked for guidance and assistance during fieldwork. Research reported in this paper was supported by Natural Environment Research Council (training grant NE/J50001X/1) to A.J.P. and National Science Foundation grant EAR0711207 to R.D.L. We thank Research Councils UK for funding the open access publication of this manuscript. The data used are listed in the references, tables, and supporting information.

References

Ambrose, T. K., K. P. Larson, C. Guilmette, J. M. Cottle, H. Buckingham, and S. Rai (2015), Lateral extrusion, underplating, and out-of-sequence thrusting within the Himalayan metamorphic core, Kanchenjunga, Nepal, *Lithosphere*, *7*, 441–464, doi:10.1130/L437.1.

Altenberger, U., and S. Wilhelm (2000), Ductile deformation of K-feldspar in dry eclogite facies shear zones in the Bergen Arcs, Norway, *Tectonophysics*, *320*, 107–121.

Bachmann, F., R. Hielscher, and H. Schaeben (2010), Texture analysis with MTEX–free and open source software toolbox, *Solid State Phenomena*, *160*, 63–68.

Baëta, R. D., and K. H. G. Ashbee (1969), Slip systems in quartz. 1. Experiments, *Ame. Mineral.*, *54*, 1551–1573.

Barber, D. J., H. C. Heard, and H. R. Wenk (1981), Deformation of dolomite single crystals from 20–800° *C, Phys. Chem. Minerals*, *7*, 271–286.

Barber, D. J., H.-R. Wenk, and H. C. Heard (1994), The plastic deformation of polycrystalline dolomite: Comparison of experimental results with theoretical predictions, *Mater. Sci. Eng. A*, *175*, 83–104.

Barth, N. C., B. R. Hacker, G. G. E. Seward, E. O. Walsh, D. Young, and S. Johnston (2010), Strain within the ultrahigh-pressure Western Gneiss region of Norway recorded by quartz CPOs, in *Continental Tectonics and Mountain Building: The Legacy of Peach and Horne*, edited by R. D. Law et al., pp. 663–685, *Geol. Soc. Spec. Publ.*, *335*.

Beaumont, C., R. A. Jamieson, M. H. Nguyen, and B. Lee (2001), Himalayan tectonics explained by extrusion of a low-viscosity crustal channel coupled to focused surface denudation, *Nature*, *414*, 738–742.

Beaumont, C., R. A. Jamieson, M. H. Nguyen, and S. Medvedev (2004), Crustal channel flows: 1. Numerical models with applications to the tectonics of the Himalayan-Tibetan orogen, *J. Geophys. Res.*, *109*, B06406, doi:10.1029/2003JB002809.

Behrmann, J. H., and J. P. Platt (1982), Sense of nappe emplacement from quartz c-axis fabrics; an example from the Betic Cordilleras (Spain), *Earth Planet. Sci. Lett.*, *59*, 208–215.

Berthé, D., P. Choukroune, and P. Jegouzo (1979), Orthogneiss, mylonite and non coaxial deformation of granites: The example of the South Armorican Shear Zone, *J. Struct. Geol.*, *1*, 31–42.

Bestmann, M., and D. J. Prior (2003), Intragranular dynamic recrystallization in naturally deformed calcite marble: Diffusion accommodated grain boundary sliding as a result of subgrain rotation recrystallization, *J. Struct. Geol.*, *25*, 1597–1613.

Beyssac, O., L. Bollinger, J. P. Avouac, and B. Goffe (2004), Thermal metamorphism in the Lesser Himalaya of Nepal determined from Raman spectroscopy of carbonaceous material, *Earth Planet. Sci. Lett.*, *225*, 233–241.

Bons, P. D., and B. den Brok (2000), Crystallographic preferred orientation development by dissolution–precipitation creep, *J. Struct. Geol.*, *22*, 1713–1722.
Bouchez, J.-L., and A. Pêcher (1981), The Himalayan Main Central Thrust pile and its quartz-rich tectonites in central Nepal, *Tectonophysics*, *78*(1), 23–50, doi:10.1016/0040-1951(81)90004-4.
Burchfiel, B. C., and L. H. Royden (1985), North-south extension within the convergent Himalayan region, *Geology*, *13*, 679–682.
Burchfiel, B. C., Z. Chen, K. V. Hodges, Y. Liu, L. H. Royden, C. Deng, and J. Xu (1992), The south Tibetan detachment system, Himalayan Orogen, *Geol. Soc. Am.*, 1–41.
Burkhard, M. (1993), Calcite twins, their geometry, appearance and significance as stress-strain markers and indicators of tectonic regime: A review, *J. Struct. Geol.*, *15*, 351–368.
Caddick, M. J., M. J. Bickle, N. B. W. Harris, T. J. B. Holland, M. S. A. Horstwood, R. R. Parrish, and T. Ahmad (2007), Burial and exhumation history of a Lesser Himalayan schist: Recording the formation of an inverted metamorphic sequence in NW India, *Earth Planet. Sci. Lett.*, *264*, 375–390.
Carosi, R., C. Montomoli, D. Rubatto, and D. Visonà (2010), Late Oligocene high-temperature shear zones in the core of the Higher Himalayan Crystallines (Lower Dolpo, western Nepal), *Tectonics*, *29*, TC4029, doi:10.1029/2008TC002400.
Carosi, R., L. Gemignani, L. Godin, S. Iaccarino, K. P. Larson, C. Montomoli, and S. M. Rai (2014), A geological journey through the deepest gorge on Earth: The Kali Gandaki valley section, west-central Nepal, in *Geological Field Trips in the Himalaya, Karakoram and Tibet*, edited by C. Montomoli, et al., *J. Virtual Explor.*, *47*(7).
Carosi, R., C. Montomoli, A. Langone, A. Turina, B. Cesare, S. Iaccarino, L. Fascioli, D. Visonà, A. Ronchi, and S. M. Rai (2015), Eocene partial melting recorded in peritectic garnets from kyanite-gneiss, Greater Himalayan Sequence, central Nepal, in *Tectonics of the Himalaya*, edited by S. Mukherjee et al.,. *Geol. Soc. Spec. Publ.*, *412*, 111–129.
Colchen, M., P. Le Fort, and A. Pêcher (1986), *Recherches Géologiques dans l'Himalaya du Népal: Annapurna-Manaslu-Ganesh Himal*, Ed. Cent. Natl. Rech. Sci., Paris.
Cole, J., B. Hacker, L. Ratschbacher, J. Dolan, G. Seward, E. Frost, and W. Frank (2007), Localized ductile shear below the seismogenic zone: Structural analysis of an exhumed strike-slip fault, Austrian Alps, *J. Geophys. Res.*, *112*, B12304, doi:10.1029/2007JB004975.
Corrie, S. L., and M. J. Kohn (2011), Metamorphic history of the central Himalaya, Annapurna region, Nepal, and implications for tectonic models, *Geol. Soc. Am. Bull.*, *123*, 1863–1879.
Cottle, J. M., K. P. Larson, and D. A. Kellett (2015), How does the mid-crust accommodate deformation in large, hot collisional orogens? A review of recent research in the Himalayan orogen, *J. Struct. Geol.*, *78*, 119–133, doi:10.1016/j.jsg.2015.06.008.
De Bresser, J. H. P., and C. J. Spiers (1997), Strength characteristics of the r, f, and c slip systems in calcite, *Tectonophysics*, *272*, 1–23.
DeCelles, P. G., G. E. Gehrels, J. Quade, B. LaReau, and M. Spurlin (2000), Tectonic implications of U-Pb zircon ages of the Himalayan orogenic belt in Nepal, *Science*, *288*, 497–499.
DeCelles, P. G., D. M. Robinson, J. Quade, T. P. Ojha, C. N. Garzione, P. Copeland, and B. N. Upreti (2001), Stratigraphy, structure, and tectonic evolution of the Himalayan fold-thrust belt in western Nepal, *Tectonics*, *20*, 487–509.
Delle Piane, C., L. Burlini, K. Kunze, P. Brack, and J. P. Burg (2008), Rheology of dolomite: Large strain torsion experiments and natural examples, *J. Struct. Geol.*, *30*, 767–776.
Delle Piane, C., L. Burlini, and K. Kunze (2009), The influence of dolomite on the plastic flow of calcite: Rheological, microstructural and chemical evolution during large strain torsion experiments, *Tectonophysics*, *467*, 145–166.
Evans, M. A., and W. M. Dunne (1991), Strain factorization and partitioning in the North Mountain thrust sheet, central Appalachians, U.S.A., *J. Struct. Geol.*, *13*, 21–35.
Faleiros, F. M., R. Moraes, M. Pavan, and G. A. C. Campanha (2016), A new empirical calibration of the quartz c-axis fabric opening-angle deformation thermometer, *Tectonophysics*, *671*, 173–182.
Ferrill, D. A., A. P. Morris, M. A. Evans, M. Burkhard, R. H. Groshong Jr., and C. M. Onasch (2004), Calcite twin morphology: A low-temperature deformation geothermometer, *J. Struct. Geol.*, *26*, 1521–1529.
Fitz Gerald, J. D., and H. Stünitz (1993), Deformation of granitoids at low metamorphic grade. I: Reactions and grain size reduction, *Tectonophysics*, *221*, 269–297.
Fukuda, J.-i., T. Okudaira, T. Satsukawa, and K. Michibayashi (2012), Solution–precipitation of K-feldspar in deformed granitoids and its relationship to the distribution of water, *Tectonophysics*, *532–535*, 175–185.
Gandais, M., and C. Willaime (1984), Mechanical properties of feldspars, in *Feldspars and Feldspathoids*, edited by W. Brown, pp. 207–246, Springer, Netherlands.
Garzione, C. N., P. G. DeCelles, D. G. Hodkinson, T. P. Ojha, and B. N. Upreti (2003), East-west extension and Miocene environmental change in the southern Tibetan plateau: Thakkhola graben, central Nepal, *Geol. Soc. Am. Bull.*, *115*, 3–20.
Godin, L. (2003), Structural evolution of the Tethyan sedimentary sequence in the Annapurna area, central Nepal Himalaya, *J. Asian Earth Sci.*, *22*, 307–328.
Godin, L., R. R. Parrish, R. L. Brown, and K. V. Hodges (2001), Crustal thickening leading to exhumation of the Himalayan metamorphic core of central Nepal: Insight from U-Pb geochronology and Ar-40/Ar-39 thermochronology, *Tectonics*, *20*, 729–747.
Godin, L., D. Grujic, R. D. Law, and M. P. Searle (2006), Channel flow, ductile extrusion and exhumation in continental collision zones: An introduction, in *Channel Flow, Ductile Extrusion and Exhumation in Continental Collision Zones*, edited by R. D. Law, M. P. Searle, and L. Godin, pp. 1–23, *Geol. Soc. Spec. Publ.*, *268*.
Grasemann, B., H. Fritz, and J. C. Vannay (1999), Quantitative kinematic flow analysis from the Main Central Thrust Zone (NW-Himalaya, India): Implications for a decelerating strain path and the extrusion of orogenic wedges, *J. Struct. Geol.*, *21*, 837–853.
Grujic, D. (2006), Channel flow and continental collision tectonics: An overview. in *Channel Flow, Ductile Extrusion and Exhumation in Continental Collision Zones*, edited by R. D. Law, M. P. Searle, and L. Godin, pp. 25–37, *Geol. Soc. Spec. Publ.*, *268*.
Grujic, D., M. Casey, C. Davidson, L. S. Hollister, R. Kundig, T. Pavlis, and S. Schmid (1996), Ductile extrusion of the Higher Himalayan Crystalline in Bhutan: Evidence from quartz microfabrics, *Tectonophysics*, *260*, 21–43.
Harrison, T. M., J. Célérier, A. B. Aikman, J. Hermann, and M. T. Heizler (2009), Diffusion of 40Ar in muscovite, *Geochimica et Cosmochimica Acta*, *73*(4), 1039–1051, doi:10.1016/j.gca.2008.09.038.
He, D., A. A. G. Webb, K. P. Larson, A. J. Martin, and A. K. Schmitt (2014), Extrusion vs. duplexing models of Himalayan mountain building 3: Duplexing dominates from the Oligocene to Present, *Int. Geol. Rev.*, *57*, 1–27.
Heidelbach, F., A. Post, and J. Tullis (2000), Crystallographic preferred orientation in albite samples deformed experimentally by dislocation and solution precipitation creep, *J. Struct. Geol.*, *22*, 1649–1661.
Hippertt, J. F. (1994), Microstructures and c-axis fabrics indicative of quartz dissolution in sheared quartzites and phyllonites, *Tectonophysics*, *229*, 141–163.

Hodges, K. V., R. R. Parrish, and M. P. Searle (1996), Tectonic evolution of the central Annapurna Range, Nepalese Himalayas, *Tectonics*, *15*, 1264–1291.
Holness, M. B., and E. W. Sawyer (2008), On the pseudomorphing of melt-filled pores during the crystallization of migmatites, *J. Petrol.*, *49*, 1343–1363.
Holness, M. B., B. Cesare, and E. W. Sawyer (2011), Melted rocks under the microscope: Microstructures and their interpretation, *Elements*, *7*, 247–252.
Hurtado, J. M., K. V. Hodges, and K. X. Whipple (2001), Neotectonics of the Thakkhola graben and implications for recent activity on the South Tibetan fault system in the central Nepal Himalaya, *Geol. Soc. Am. Bull.*, *113*, 222–240.
Iaccarino, S., C. Montomoli, R. Carosi, H. J. Massonne, A. Langone, and D. Visonà (2015), Pressure-temperature-time-deformation path of kyanite-bearing migmatitic paragneiss in the Kali Gandaki valley (Central Nepal): Investigation of Late Eocene-Early Oligocene melting processes, *Lithos*, *231*, 103–121.
Ihinger, P. D., and S. I. Zink (2000), Determination of relative growth rates of natural quartz crystals, *Nature*, *404*, 865–869.
Jamieson, R. A., and C. Beaumont (2013), On the origin of orogens, *Geol. Soc. Am. Bull.*, *125*, 1671–1702.
Jamieson, R. A., C. Beaumont, S. Medvedev, and M. H. Nguyen (2004), Crustal channel flows: 2. Numerical models with implications for metamorphism in the Himalayan-Tibetan orogen, *J. Geophys. Res.*, *109*, B06407, doi:10.1029/2003JB002811.
Jamieson, R. A., M. J. Unsworth, N. B. W. Harris, C. L. Rosenberg, and K. Schulmann (2011), Crustal melting and the flow of mountains, *Elements*, *7*, 253–260.
Jessup, M. J., R. D. Law, M. P. Searle, and M. S. Hubbard (2006), Structural evolution and vorticity of flow during extrusion and exhumation of the Greater Himalayan Slab, Mount Everest Massif, Tibet/Nepal: Implications for orogen-scale flow partitioning, in *Channel Flow, Ductile Extrusion and Exhumation in Continental Collision Zones*, edited by R. D. Law, M. P. Searle, L. Godin, *Geol. Soc. Spec. Publ.*, *268*, 379–413.
Kaneko, Y. (1995), Thermal structure in the Annapurna region, central Nepal Himalaya: Implication for the inverted metamorphism, *J. Mineral. Petrol. Econ. Geol.*, *90*, 143–154.
Khanal, S., D. M. Robinson, S. Mandal, and P. Simkhada (2015), Structural, geochronological and geochemical evidence for two distinct thrust sheets in the 'Main Central thrust zone', the Main Central thrust and Ramgarh–Munsiari thrust: Implications for upper crustal shortening in central Nepal, in *Tectonics of the Himalaya*, edited by S. *Mukherjee, Geol. Soc. Spec. Publ.*, *412*, 221–245.
Knipe, R. J., and R. D. Law (1987), The influence of crystallographic orientation and grain boundary migration on microstructural and textural evolution in an S-C mylonite, *Tectonophysics*, *135*, 155–169.
Kohn, M. J. (2008), P-T-t data from central Nepal support critical taper and repudiate large-scale channel flow of the Greater Himalayan Sequence, *Geol. Soc. Am. Bull.*, *120*, 259–273.
Kohn, M. J., and S. L. Corrie (2011), Preserved Zr-temperatures and U–Pb ages in high-grade metamorphic titanite: Evidence for a static hot channel in the Himalayan orogen, *Earth Planet. Sci. Lett.*, *311*, 136–143.
Kruhl, J. H. (1996), Prism- and basal-plane parallel subgrain boundaries in quartz: A microstructural geothermobarometer, *J. Metamorph. Geol.*, *46*, 581–586.
Kruhl, J. H. (1998), Reply: Prism- and basal-plane parallel subgrain boundaries in quartz: A microstructural geothermobarometer, *J. Metamorph. Geol.*, *16*, 142–146.
Lafrance, B., J. C. White, and P. F. Williams (1994), Natural calcite c-axis fabrics: An alternate interpretation, *Tectonophysics*, *229*, 1–18.
Larson, K. P., and J. M. Cottle (2014), Midcrustal discontinuities and the assembly of the Himalayan midcrust, *Tectonics*, *33*, 718–740, doi:10.1002/2013TC003452.
Larson, K. P., and J. M. Cottle (2015), Initiation of crustal shortening in the Himalaya, *Terra Nova*, *27*, 169–174.
Larson, K. P., and L. Godin (2009), Kinematics of the Greater Himalayan sequence, Dhaulagiri Himal: Implications for the structural framework of central Nepal, *J. Geol. Soc.*, *166*, 25–43.
Larson, K. P., L. Godin, and R. A. Price (2010), Relationships between displacement and distortion in orogens: Linking the Himalayan foreland and hinterland in central Nepal, *Geol. Soc. Am. Bull.*, *122*, 1116–1134.
Larson, K. P., T. K. Ambrose, A. A. G. Webb, J. M. Cottle, and S. Shrestha (2015), Reconciling Himalayan midcrustal discontinuities: The Main Central thrust system, *Earth Planet. Sci. Lett.*, *429*, 139–146.
Law, R. D. (2014), Deformation thermometry based on quartz c-axis fabrics and recrystallization microstructures: A review, *J. Struct. Geol.*, *66*, 129–161.
Law, R. D., M. P. Searle, and R. L. Simpson (2004), Strain, deformation temperatures and vorticity of flow at the top of the Greater Himalayan Slab, Everest Massif, Tibet, *J. Geol. Soc.*, *161*, 305–320.
Law, R. D., M. J. Jessup, M. P. Searle, M. K. Francsis, D. J. Walters, and J. M. Cottle (2011), Telescoping of isotherms beneath the South Tibetan detachment system, Mount Everest Massif, *J. Struct. Geol.*, *33*, 1569–1594.
Law, R. D., D. W. Stahr III, M. K. Francsis, K. T. Ashley, B. Grasemann, and T. Ahmad (2013), Deformation temperatures and flow vorticities near the base of the Greater Himalayan Series, Sutlej Valley and Shimla Klippe, NW India, *J. Structural Geology*, *54*, 21–53, doi:10.1016/j.jsg.2013.05.009.
Le Fort, P. (1975), Himalayas: The collided range. Present knowledge of the continental arc, *Am. J. Sci.*, *275-A*, 1–44.
Le Fort, P., A. Pêcher, and B. N. Upreti (1987), A section through the Tibetan Slab in Central Nepal (Kali Gandaki valley): Mineral chemistry and thermobarometry of the Main Central Thrust zone, in *Orogenic Evolution of Southern Asia (from Turkey to Indonesia)*, edited by P. Le Fort, M. Colchen, and C. Montenat, pp. 211–228, Sci. de la Terre, Nancy, France.
Leiss, B., and D. J. Barber (1999), Mechanisms of dynamic recrystallization in naturally deformed dolomite inferred from EBSP analyses, *Tectonophysics*, *303*, 51–69.
Leiss, B., and G. Molli (2003), 'High-temperature' texture in naturally deformed Carrara marble from the Alpi Apuane, Italy, *J. Struct. Geol.*, *25*, 649–658.
Linker, M. F., S. H. Kirby, A. Ord, and J. M. Christie (1984), Effects of compression direction on the plasticity and rheology of hydrolytically weakened synthetic quartz crystals at atmospheric pressure, *J. Geophys. Res.*, *89*, 4241–4255.
Lister, G. S. (1977), Discussion: Crossed-girdle c-axis fabrics in quartzites plastically deformed by plane strain and progressive simple shear, *Tectonophysics*, *39*, 51–54.
Lister, G. S., M. S. Paterson, and B. E. Hobbs (1978), The simulation of fabric development in plastic deformation and its application to quartzite: The model, *Tectonophysics*, *45*(2), 107–158, doi:10.1016/0040-1951(78)90004-5.
Lister, G. S., and B. E. Hobbs (1980), The simulation of fabric development during plastic deformation and its application to quartzite: The influence of deformation history, *J. Struct. Geol.*, *2*, 355–370.
Lister, G. S., and P. F. Williams (1979), Fabric development in shear zones: Theoretical controls and observed phenomena, *J. Struct. Geol.*, *1*, 283–297.

Little, T. A., B. R. Hacker, S. J. Brownlee, and G. Seward (2013), Microstructures and quartz lattice-preferred orientations in the eclogite-bearing migmatitic gneisses of the D'Entrecasteaux Islands, Papua New Guinea, *Geochem. Geophys. Geosyst.*, *14*, 2030–2062, doi:10.1002/ggge.20132.
Lloyd, G. E. (1987), Atomic number and crystallographic contrast images with the SEM: A review of backscattered electron techniques, *Mineral. Mag.*, *51*, 3–19.
Lloyd, G. E., and B. Freeman (1994), Dynamic recrystallization of quartz under greenschist conditions, *J. Struct. Geol.*, *16*, 867–881.
Lloyd, G. E., R. D. Law, D. Mainprice, and J. Wheeler (1992), Microstructural and crystal fabric evolution during shear zone formationm, *J. Struct. Geol.*, *14*, 1079–1100.
Mainprice, D., J.-L. Bouchez, P. Blumenfeld, and J. M. Tubià (1986), Dominant c slip in naturally deformed quartz: Implications for dramatic plastic softening at high temperature, *Geology*, *14*, 819–822.
Martin, A. J., J. Ganguly, and P. G. DeCelles (2010), Metamorphism of Greater and Lesser Himalayan rocks exposed in the Modi Khola valley, central Nepal, *Contrib. Mineral. Petrol.*, *159*, 203–223.
Martin, A. J., P. Copeland, and J. A. Benowitz (2015), Muscovite 40Ar/39Ar ages help reveal the Neogene tectonic evolution of the southern Annapurna Range, central Nepal, in *Tectonics of the Himalaya*, edited by S. Mukherjee et al., *Geol. Soc. Spec. Publ.*, *412*, doi:10.1144/SP412.5.
Means, W. D. (1981), The concept of steady-state foliation, *Tectonophysics*, *78*, 179–199.
Menegon, L., G. Pennacchioni, and R. Spiess (2008), Dissolution-precipitation creep of K-feldspar in mid-crustal granite mylonites, *J. Struct. Geol.*, *30*, 565–579.
Montomoli, C., S. Iaccarino, R. Carosi, A. Langone, and D. Visona (2013), Tectonometamorphic discontinuities within the greater Himalayan Sequence in Western Nepal (Central Himalaya): Insights on the exhumation of crystalline rocks, *Tectonophysics*, *608*, 1349–1370.
Montomoli, C., R. Carosi, and S. Iaccarino (2015), Tectonometamorphic discontinuities in the Greater Himalayan Sequence: A local or a regional feature?, in *Tectonics of the Himalaya*, edited by S. Mukherjee et al., *Geol. Soc. Spec. Publ.*, *412*, 25–41.
Morgan, S. S., and R. D. Law (2004), Unusual transition in quartzite dislocation creep regimes and crystal slip systems in the aureole of the Eureka Valley–Joshua Flat–Beer Creek pluton, California: A case for anhydrous conditions created by decarbonation reactions, *Tectonophysics*, *384*, 209–231.
Mottram, C. M., C. J. Warren, D. Regis, N. M. W. Roberts, N. B. W. Harris, T. W. Argles, and R. R. Parrish (2014), Developing an inverted Barrovian sequence; insights from monazite petrochronology, *Earth Planet. Sci. Lett.*, *403*, 418–431.
Mottram, C. M., R. R. Parrish, D. Regis, C. J. Warren, T. W. Argles, N. B. W. Harris, and N. M. W. Roberts (2015), Using U-Th-Pb petrochronology to determine rates of ductile thrusting: Time windows into the Main Central Thrust, Sikkim Himalaya, *Tectonics*, *34*, 1355–1374, doi: 10.1002/2014TC003743.
Mukherjee, S. (2013), Higher Himalaya in the Bhagirathi section (NW Himalaya, India): Its structures, backthrusts and extrusion mechanism by both channel flow and critical taper mechanisms, *Int. J. Earth Sci.*, *102*, 1851–1870.
Mukherjee, S. (2015), A review on out-of-sequence deformation in the Himalaya, in *Tectonics of the Himalaya*, edited by S. Mukherjee et al., *Geol. Soc. Spec. Publ.*, *412*(1), 67–109, doi:10.1144/sp412.13.
Nazarchuk, J. H. (1993), Structure and geochronology of the Greater Himalaya, Kali Gandaki region, west-central Nepal, MS thesis, Carleton Univ., Ottawa, Ontario.
Nicolas, A., and J.-P. Poirier (1976), *Crystalline Plasticity and Solid State Flow in Metamorphic Rocks*, John Wiley, London, U. K.
Olsen, T. S., and D. L. Kohlstedt (1985), Natural deformation and recrystallization of some intermediate plagioclase feldspars, *Tectonophysics*, *111*, 107–131.
Parsons, A. J., R. D. Law, M. P. Searle, R. J. Phillips, and G. E. Lloyd (2016a), Geology of the Dhaulagiri-Annapurna-Manaslu Himalaya, Western Region, Nepal. 1:200,000, *J. Maps*, *12*, 100–110.
Parsons, A. J., R. J. Phillips, G. E. Lloyd, R. D. Law, M. P. Searle, and R. D. Walshaw (2016b), Mid-crustal deformation of the Annapurna-Dhaulagiri Himalaya, central Nepal: An atypical example of channel flow during the Himalayan orogeny, *Geosphere*, *12*(3), 1–31, doi: 10.1130/GES01246.1.
Passchier, C. W., and R. A. J. Trouw (2005), *Microtectonics*, 2nd ed, Springer, N. Y.
Paudel, L. P., and K. Arita (2006), Thermal evolution of the Lesser Himalaya, central Nepal: Insights from K-white micas compositional variation, *Gondwana Res.*, *9*, 409–425.
Pêcher, A., and P. Le Fort (1977), Origin and significance of the Lesser Himalayan augen gneisses, Himalaya Sciences dela Terre, *Coll Int. C. N. R. S*, *268*, 295–329.
Pieri, M., K. Kunze, L. Burlini, I. Stretton, D. L. Olgaard, J. P. Burg, and H. R. Wenk (2001), Texture development of calcite by deformation and dynamic recrystallization at 1000°K during torsion experiments of marble to large strains, *Tectonophysics*, *330*, 119–140.
Prior, D. J., et al. (1999), The application of electron backscatter diffraction and orientation contrast imaging in the SEM to textural problems in rocks, *Am. Mineral.*, *84*, 1741–1759.
Robinson, D. M., and A. J. Martin (2014), Reconstructing the Greater Indian margin: A balanced cross section in central Nepal focusing on the Lesser Himalayan duplex, *Tectonics*, *33*, 2143–2168, doi: 10.1002/2014TC003564.
Robinson, D. M., P. G. DeCelles, and P. Copeland (2006), Tectonic evolution of the Himalayan thrust belt in western Nepal: Implications for channel flow models, *Geol. Soc. Am. Bull.*, *118*, 865–885.
Rosenberg, C. L., and H. Stünitz (2003), Deformation and recrystallization of plagioclase along a temperature gradient: An example from the Bergell tonalite, *J. Struct. Geol.*, *25*, 389–408.
Rosenberg, C. L., S. Medvedev, and M. Handy (2007), Effects of melting on faulting and continental deformation, in *Tectonic Faults, Agents of Change on a Dynamic Earth*, edited by M. R. Handy, G. Hirth, and N. Hovius, pp. 357–401, MIT Press, Cambridge, Mass.
Sawyer, E. W. (2008), *Atlas of Migmatites. The Canadian Mineralogist, Spec. Publ. 9*, Ottawa, Ontario, NRC Res. Press and Mineral. Assoc. of Can, 371 pp.
Schmid, S. M., and M. Casey (1986), Complete fabric analysis of some commonly observed quartz c-axis patterns, in *Mineral and Rock Deformation: Laboratory Studies: The Paterson Volume*, edited by B. E. Hobbs and H. C. Heard, pp. 263–286, *AGU Monogr.*, *36*.
Schulmann, K., B. Mlčoch, and R. Melka (1996), High-temperature microstructures and rheology of deformed granite, Erzgebirge, Bohemian Massif, *J. Struct. Geol.*, *18*, 719–733.
Searle, M. P. (1986), Structural evolution and sequence of thrusting in the High Himalayan, Tibetan-Tethys and Indus Suture zones of Zanskar and Ladakh, Western Himalaya, *J. Struct. Geol.*, *8*, 923–936.
Searle, M. P. (2010), Low-angle normal faults in the compressional Himalayan orogen: Evidence from the Annapurna-Dhaulagiri Himalaya, Nepal, *Geosphere*, *6*, 296–315.
Searle, M. P. (2015), Mountain building, tectonic evolution, rheology and crustal flow in the Himalaya, Karakorum and Tibet, in *Treatise on Geophysics*, 2nd ed., vol. 6, edited by G. Schubert, pp. 469–511, Elsevier, Oxford, U. K.
Searle, M. P., and L. Godin (2003), The South Tibetan Detachment and the Manaslu Leucogranite: A Structural Reinterpretation and Restoration of the Annapurna-Manaslu Himalaya, Nepal, *J. Geol.*, *111*(5), 505–523, doi:10.1086/376763.

Searle, M. P., R. L. Simpson, R. D. Law, R. R. Parrish, and D. J. Waters (2003), The structural geometry, metamorphic and magmatic evolution of the Everest massif, High Himalaya of Nepal-South Tibet, *J. Geol. Soc. London*, *160*, 345–366.

Searle, M. P., R. D. Law, and M. J. Jessup (2006), Crustal structure, restoration and evolution of the Greater Himalaya in Nepal-South Tibet: Implications for channel flow and ductile extrusion of the middle crust, in *Channel Flow, Ductile Extrusion and Exhumation in Continental Collision Zones*, edited by R. D. Law, M. P. Searle, and L. *Godin, Geol. Soc. Spec. Publ.*, *268*, 355–378.

Searle, M. P., J. M. Cottle, M. J. Streule, and D. J. Waters (2010), Crustal melt granites and migmatites along the Himalaya: Melt source, segregation, transport and granite emplacement mechanisms, in *Sixth Hutton Symposium on the Origin of Granites and Related Rocks: Proceedings of a Symposium, Transactions of the Royal Society of Edinburgh*, *Earth Sci.*, *100*, 219–233.

Searle, M. P., J. R. Elliott, R. J. Phillips, and S. L. Chung (2011), Crustal-lithospheric structure and continental extrusion of Tibet, *J. Geol. Soc.*, *168*, 633–672.

Spencer, C. J., R. A. Harris, and M. J. Dorais (2012), The metamorphism and exhumation of the Himalayan metamorphic core, eastern Garhwal region, India, *Tectonics*, *31*, TC1007, doi:10.1029/2010TC002853.

Srivastava, P., and G. Mitra (1994), Thrust geometries and deep structure of the outer and lesser Himalaya, Kumaon and Garhwal (India): Implications for evolution of the Himalayan fold-and-thrust belt, *Tectonics*, *13*, 89–109.

Stallard, A., and D. Shelley (1995), Quartz c-axes parallel to stretching directions in very low-grade metamorphic rocks, *Tectonophysics*, *249*, 31–40.

Stipp, M., H. Stunitz, R. Heilbronner, and S. M. Schmid (2002), The eastern Tonale fault zone: A 'natural laboratory' for crystal plastic deformation of quartz over a temperature range from 250 to 700 degrees C, *J. Struct. Geol.*, *24*, 1861–1884.

Stünitz, H., J. D. Fitz Gerald, and J. Tullis (2003), Dislocation generation, slip systems, and dynamic recrystallization in experimentally deformed plagioclase single crystals, *Tectonophysics*, *372*, 215–233.

Trullenque, G., K. Kunze, R. Heilbronner, H. Stünitz, and S. M. Schmid (2006), Microfabrics of calcite ultramylonites as records of coaxial and non-coaxial deformation kinematics: Examples from the Rocher de l'Yret shear zone (Western Alps), *Tectonophysics*, *424*, 69–97.

Tullis, J., and R. A. Yund (1991), Diffusion creep in feldspar aggregates: Experimental evidence, *J. Struct. Geol.*, *13*, 987–1000.

Valdiya, K. S. (1980), *Geology of Kumaun Lesser Himalaya*. Himachal Press, Wadia Inst. of Himalayan Geol., Dehra Dun, India.

Vannay, J. C., and K. V. Hodges (1996), Tectonometamorphic evolution of the Himalayan metamorphic core between the Annapurna and Dhaulagiri, central Nepal, *J. Metamorph. Geol.*, *14*, 635–656.

Wallis, D., R. J. Phillips, and G. E. Lloyd (2014), Evolution of the Eastern Karakoram Metamorphic Complex, Ladakh, NW India, and its relationship to magmatism and regional tectonics, *Tectonophysics*, *626*, 41–52.

Wallis, D., G. E. Lloyd, R. J. Phillips, A. J. Parsons, and R. D. Walshaw (2015), Low effective fault strength due to frictional-viscous flow in phyllonites, Karakoram Fault Zone, NW India, *J. Struct. Geol.*, *77*, 45–61.

Wang, J. M., J. J. Zhang, and X. X. Wang (2013), Structural kinematics, metamorphic P–T profiles and zircon geochronology across the Greater Himalayan Crystalline Complex in south-central Tibet: Implication for a revised channel flow, *J. Metamorph. Geol.*, *31*, 607–628.

Weber, J. C., D. A. Ferrill, and M. K. Roden-Tice (2001), Calcite and quartz microstructural geothermometry of low-grade metasedimentary rocks, Northern Range, Trinidad, *J. Struct. Geol.*, *23*, 93–112.

Wenk, H. R., and J. Shore (1975) Preferred orientation in experimentally deformed dolomite, *Contrib. Mineral Petrol.*, *50*, 115–126.

Wenk, H. R., T. Takeshita, E. Bechler, B. G. Erskine, and S. Matthies (1987), Pure shear and simple shear calcite textures. Comparison of experimental, theoretical and natural data, *J. Struct. Geol.*, *9*, 731–745.

White, R. W., R. Powell, and T. J. B. Holland (2001), Calculation of partial melting equilibria in the system Na2O–CaO–K2O–FeO–MgO–Al2O3–SiO2–H2O (NCKFMASH), *J. Metamorph. Geol.*, *19*, 139–153.

Williams, P. F., D. Jiang, and S. Lin (2006), Interpretation of deformation fabrics of infrastructure zone rocks in the context of channel flow and other tectonic models, in *Channel Flow, Ductile Extrusion and Exhumation in Continental Collision Zones*, edited by R. D. Law, M. P. Searle, and L. Godin, pp. 221–235, *Geol. Soc. Spec. Publ.*, *268*.

Yakymchuk, C., and L. Godin (2012), Coupled role of deformation and metamorphism in the construction of inverted metamorphic sequences: an example from far-northwest Nepal. *J. Metamorphic Geology*, *30*, 513–535, doi:10.1111/j.1525-1314.2012.00979.x